Journal of South American Earth Sciences 119 (2022) 103991

Contents lists available at ScienceDirect

Journal of South American Earth Sciences

journal homepage: www.elsevier.com/locate/jsames

Ultramafic-hosted volcanogenic massive sulfide deposits from Cuban ophiolites☆

Diego Domínguez-Carretero [a,*], Joaquín A. Proenza [a], José María González-Jiménez [b], Angélica I. Llanes-Castro [c], Harlison Torres [d], Thomas Aiglsperger [e], Lisard Torró [f], Carbeny Capote [c], Deysy de la Nuez [c], Antonio Garcia-Casco [b,g]

[a] Departament de Mineralogia, Petrologia i Geologia Aplicada, Facultat de Ciències de la Terra, Universitat de Barcelona, Spain
[b] Instituto Andaluz de Ciencias de la Tierra, CSIC-Universidad de Granada, Avda. de las Palmeras 4, 18100 Armilla, Granada, Spain
[c] Institute of Geology and Paleontology, Vía Blanca, Línea del Ferrocarril s/n, San Miguel del Padrón, Havana, 10200, Cuba
[d] DataRock Ingeniería SAS, Calle 42 # 63A-198, Medellín, Colombia
[e] Department of Civil Engineering and Natural Resources, Luleå University of Technology, Sweden
[f] Geological Engineering Program, Faculty of Sciences and Engineering, Pontifical Catholic University of Peru (PUCP), Peru
[g] Departamento de Mineralogía y Petrología, Facultad de Ciencias, Universidad de Granada, Spain

ARTICLE INFO

Keywords:
Ultramafic-hosted volcanogenic massive sulfide deposits (UM-VMS)
Ophiolite
Cuba
Supra-subduction zone (SSZ)
Serpentinization
Gold

ABSTRACT

Ultramafic-hosted volcanogenic massive sulfide deposits (UM-VMS) located in the Havana-Matanzas ophiolite (Cuba) are the only known example of this type of mineralization in the Caribbean realm. UM-VMS from Havana-Matanzas are enriched in Cu, Ni, Co, Au, and Ag. The mineralization consists of massive sulfide bodies mostly composed of pyrrhotite and hosted by serpentinized upper mantle peridotites. Chemical composition of unaltered cores in Cr-spinel grains found within the massive sulfide mineralization and in the peridotite host indicates formation in the fore-arc region of the Greater Antilles volcanic arc. A first stage of serpentinization probably took place prior to the sulfide mineralization event. The UM-VMS mineralization formed by the near-complete replacement of the silicate assemblage of partially serpentinized peridotites underneath the seafloor. The sequence of sulfide mineralization has been divided into two stages. The first stage is characterized by a very reduced hydrothermal mineral assemblage consisting of pyrrhotite, Co–Ni–Fe diarsenides, chalcopyrite, Co-rich pentlandite, and electrum. In the second stage, pyrite and Co–Ni–Fe sulfarsenides partially replaced pyrrhotite and diarsenides, respectively, under a more oxidizing regime during the advanced stages of ongoing serpentinization. The proposed conceptual genetic model presented here can be useful for future exploration targeting this type of deposit in the Caribbean region and elsewhere.

Author contribution

Carbeny Capote: Writing – review & editing. Deysy de-la-Nuez: Writing – review & editing. Antonio Garcia-Casco: Writing – review & editing, Supervision. Diego Domínguez-Carretero: Writing – original draft, Investigation. Joaquín A. Proenza: Writing – review & editing, Supervision, Methodology, Conceptualization. José María González-Jiménez: Writing – review & editing, Supervision. Angélica I. Llanes-Castro: Writing – review & editing. Harlison Torres: Writing – review & editing. Thomas Aiglsperger: Writing – review & editing. Lisard Torró: Writing – review & editing, Conceptualization

1. Introduction

Oceanographic campaigns unveiled multiple occurrences of seafloor massive sulfide deposits (SMS) hosted in variably altered ultramafic rocks along slow or ultraslow spreading ridges with a low magmatic budget (Fouquet et al., 2010). These ultramafic-hosted SMS (UM-SMS) occur mostly in the footwall of low-angle detachment faults such as in mid-ocean ridges (MOR; Escartín et al., 2008), ocean-continent transition (OCT; Haupert et al., 2016) and supra-subduction zones settings (SSZ; Maffione et al., 2015; Morris et al., 2017), although they may also form in the volcanic, intrusive, and sedimentary rocks of the

☆ To be submitted to Special issue "Developments in mineral deposits and metallogeny in Latin America" of Journal of South American Earth Sciences.

* Corresponding author.
E-mail address: ddominguezcarretero@ub.edu (D. Domínguez-Carretero).

https://doi.org/10.1016/j.jsames.2022.103991
Received 13 May 2022; Received in revised form 22 July 2022; Accepted 16 August 2022
Available online 23 August 2022

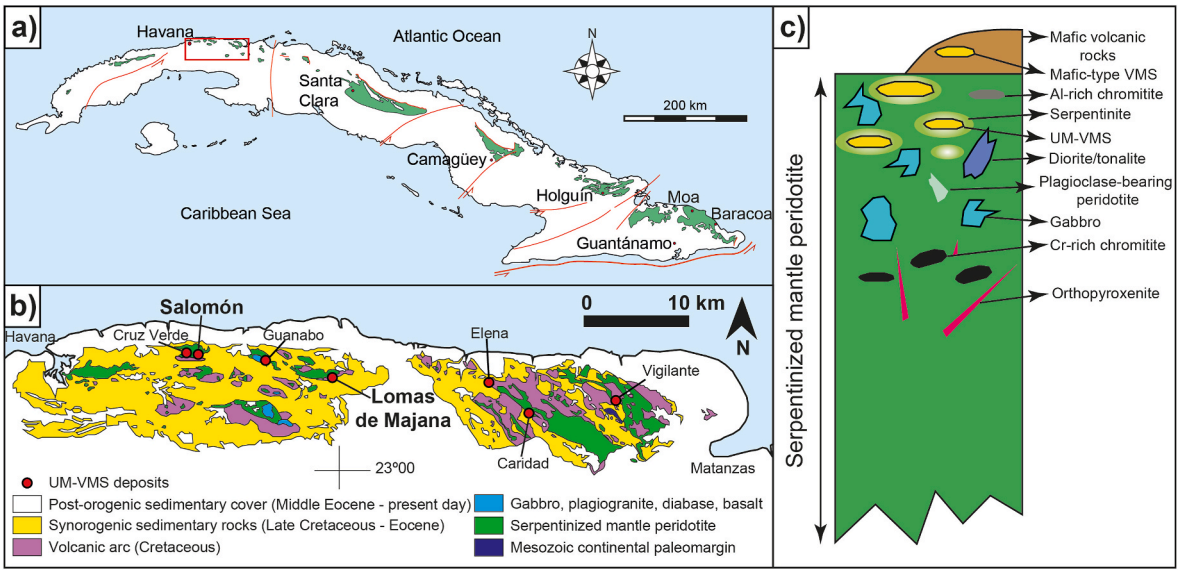

Fig. 1. a) Geological map showing the location of the Cuban Ophiolitic Belt (modified from Iturralde-Vinent et al., 2016). The red rectangle marks the location of the Havana-Matanzas ophiolite; b) geological map of the Havana-Matanzas ophiolite with the location of all known UM-VMS deposits (modified from Llanes-Castro et al., 2019); c) Schematic stratigraphic column of the Havana-Matanzas ophiolite including mineralization types. Note the scarcity of the lower crustal section (gabbros) of a typical ophiolitic ensemble.

hanging-wall of the detachment faults, close to ultramafic rocks (Petersen et al., 2009; Fouquet et al., 2010; Melekestseva et al., 2014; Patten et al., 2022). UM-SMS are mostly documented in the vicinity of MOR such as the Mid-Atlantic Ridge (e.g., Ashadze site – Mozgova et al., 2008; Rainbow site – Marques et al., 2007; Logatchev site – Petersen et al., 2009; Semenov site – Melekestseva et al., 2014) or the Southwest Indian Ridge (e.g., Tao et al., 2014; Liao et al., 2018; Ding et al., 2021). Previous research targeting basalt-hosted SMS located along magmatic spreading centers probably precluded realistic approximation to the actual number of UM-SMS, as they can be located as far as several km off-axis (Melchert et al., 2008). For example, the high-temperature (>300 °C) Logatchev vent field and the iconic low-temperature (<100 °C) Lost City hydrothermal field occur 12 km and 15 km off-axis, respectively (Fouquet et al., 2010).

Similar to their modern-day SMS equivalents, the relative abundance of fossil ultramafic-hosted volcanogenic massive sulfide deposits (UM-VMS) may be also underestimated (Patten et al., 2022). In the geological record, UM-VMS deposits are mostly documented in ocean-continent transition zones (OCT) and SSZ (Patten et al., 2022). These two settings are more likely to be tectonically emplaced on land during collisional events, thus having a greater chance of preservation relative to lithosphere and UM-VMS formed in MOR environments. Both UM-SMS and UM-VMS are typically enriched in precious (Au–Ag), critical (Co), and base metals (Cu–Ni) compared with SMS and VMS hosted by MOR basalts (MORB) or oceanic sediments (Monecke et al., 2016; Patten et al., 2022; Torró et al., 2022). Both, the particular formation environment and metalliferous signature of UM-VMS, in addition to the distinctive ultramafic nature of the host rock, make the case for the definition of a stand-alone sub-group of VMS deposits (Patten et al., 2022) supported by descriptions of preserved examples to produce tailored metallogenic models to guide exploration.

The Caribbean region contains a significant diversity of VMS deposits scattered especially across Cuba and La Hispaniola (Dominican Republic and Haiti) islands (Nelson et al., 2011 and references therein) including mafic (e.g., Júcaro or Buena Vista deposits in Cuba; Russell et al., 2000) and bimodal mafic-felsic (e.g., El Cobre in Cuba; Cerro de Maimón, La Lechoza, and Romero in the Dominican Republic; Russell et al., 2000; Cazañas et al., 2008; Torró et al., 2016, 2017, 2018) types. In addition, UM-VMS deposits have been documented in the Havana-Matanzas ophiolites stretching across the northwestern half of central Cuba. These deposits, initially known as "*minas de cobre de San Francisco de La Habana*" or "*minas de Guacaranao*" have been intermittently exploited for copper and gold since the 1580's (Ortega, 1917; Díaz-Martínez, 2010). According to Genkin et al. (1990) and Llanes-Castro (2016), these deposits are enriched in Cu (0.51–2%), Ni (0.36%), Co (0.06%), Au (0.15–10 ppm), and Ag (2.2–29.4 ppm). The genesis of these deposits remains unclear, being classified either as intermediate temperature hydrothermal (Zasietalev and Stepanov, 1966; Semionov et al., 1968; Morales, 1987; Genkin et al., 1990; Llanes et al., 2001), VMS (Abdullin et al., 1999) or orogenic Cu–Ni–Co ± Au deposits (Torres-Zafra and Cazañas, 2021).

This contribution carefully examines the field relationships, mineralogy, textures, and mineral composition of UM-VMS of the Havana-Matanzas ophiolite aiming at clarifying the relationship existing between the sulfide mineralization and ultramafic hosts. From this information, we address the environment and geodynamic setting of formation of the massive sulfide mineralization and provide a conceptual genetic model amenable for future exploration targeting in the Caribbean region and elsewhere.

2. Geological setting

2.1. 1. Ophiolites of Havana-Matanzas

Cuba hosts the largest and most abundant exposures of ophiolitic rocks across the Caribbean region, which are collectively grouped into the so-called Northern and Eastern Cuba ophiolitic belts (Fig. 1a). Both belts are tectonically discontinuous. Extending for over 1000 km and with a general E-W orientation, they exhibit discrete and variously sized mafic and ultramafic bodies with locally associated bodies of serpentinite-matrix mélanges bearing subduction-related high-pressure blocks (Iturralde-Vinent, 1996; Garcia-Casco et al., 2006; Lewis et al., 2006; Iturralde-Vinent et al., 2016). As part of the Greater Antillean orogenic belt, the Cuban Ophiolitic Belt was obducted onto the North American plate as a result of the Late Cretaceous to Mid Eocene collision between the Caribbean volcanic arc and the passive continental margins of the Bahamas and the Maya block (Iturralde-Vinent, 1996, 1998; García-Casco et al., 2008; Iturralde-Vinent et al., 2008, 2016). The

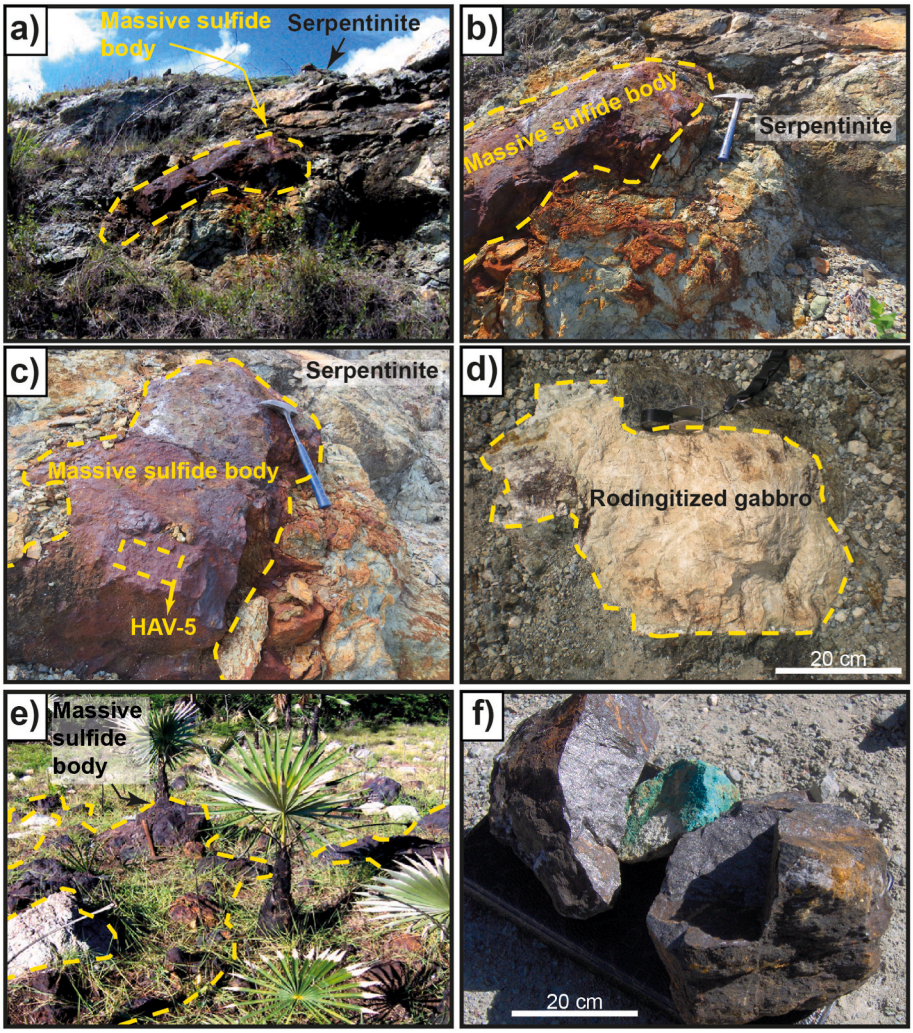

Fig. 2. a-c) Massive sulfide lenses hosted within the serpentinite host rocks at the Lomas de Majana deposit; d) Rodingitized gabbro crosscutting serpentinites at the Lomas de Majana deposits; e) Massive sulfide blocks at the Salomón mine dumps; f) Sample of massive sulfides taken from the mine dump of the Salomón mine.

ophiolite assemblages include variably serpentinized ultramafic and mafic rocks (harzburgites, dunites, wehrlites, plagioclase- and clinopyroxene-bearing peridotites, gabbro sills and dikes) from the mantle and the Moho Transition Zone (MTZ) and oceanic crustal rocks (layered and isotropic gabbros, dikes and volcanic and sedimentary rocks). Petrological, geochemical, and geochronological data suggest that Cuban ophiolites were predominantly formed in a SSZ setting, specifically in fore-arc and back-arc spreading centers (Proenza et al., 1999; Marchesi et al., 2006; Iturralde-Vinent et al., 2016; Farré-de-Pablo et al., 2020; Rui et al., 2021).

As part of the Cuban Ophiolitic Belt, the Havana-Matanzas Ophiolitic Massif is located in the west-central part of Cuba (Fig. 1a). This massif contains ENE-WSW-trending ophiolitic bodies with individual outcropping areas less than 60 km^2 (Palmer, 1945; Brönniman and Rigassi, 1963). Mafic and ultramafic bodies in the Havana-Matanzas Ophiolitic Massif constitute a complete but tectonically discontinuous ophiolitic sequence with a restored thickness of about 4 km (Linares et al., 1985). The massif is tectonically imbricated with Cretaceous intra-oceanic volcanic arc units and Campanian to Maastrichtian synorogenic sedimentary sequences (Llanes-Castro et al., 2015a, 2019). All these units constitute an allochthonous nappe stack that overrides tectonic units of the passive continental margin of North America (Bahamas; Iturralde--Vinent, 2021). The ophiolitic sequence comprises upper mantle peridotites (serpentinized harzburgites with common orthopyroxenite veins and bodies, minor sub-concordant dunites, and chromitite bodies), rocks from the MTZ (plagioclase- and clinopyroxene-bearing peridotites, gabbro sills, and pegmatitic gabbro dikes) and a poorly exposed crustal section (massive gabbros, dolerites, and volcanic rocks with island-arc tholeiitic and boninitic affinities; Fig. 1b–c) (Fonseca et al., 1985; Kerr et al., 1999; Llanes et al., 2001; Llanes et al., 2015b). Fault-bounded peridotite bodies include gabbros, plagiogranites, tonalites, and diorites (Llanes-Castro et al., 2019). In addition, the Havana-Matanzas Ophiolitic Massif hosts several mineralization types including Al- and Cr-rich chromitites, mafic-type VMS, and Au-rich UM-VMS (Fig. 1c). In this paper we focus on the latter mineralization type.

2.2. *Geology of the UM-VMS deposits of the Havana-Matanzas Ophiolitic Massif*

The Havana-Matanzas Ophiolitic Massif hosts the only UM-VMS mining district in the Caribbean region. Seven different deposits have been documented: Lomas de Majana, Salomón, Cruz Verde, Guanabo, Elena, Caridad, and Vigilante (Fig. 1b) (Abdullin et al., 1999; Llanes et al., 2001; Cazanas et al., 2017). In the present work, we have studied the Lomas de Majana and Salomón deposits (Figs. 2 and 3). The mineralization is zoned and grades from massive sulfide bodies (Fig. 2a, c-d) to sulfide-serpentinite banded ores and, finally, to sulfide disseminations and veinlets within the serpentinized peridotite host (Genkin et al., 1990). The massive sulfide lenses are up to 50 m in length and 5 m in width and are hosted by highly serpentinized harzburgites and

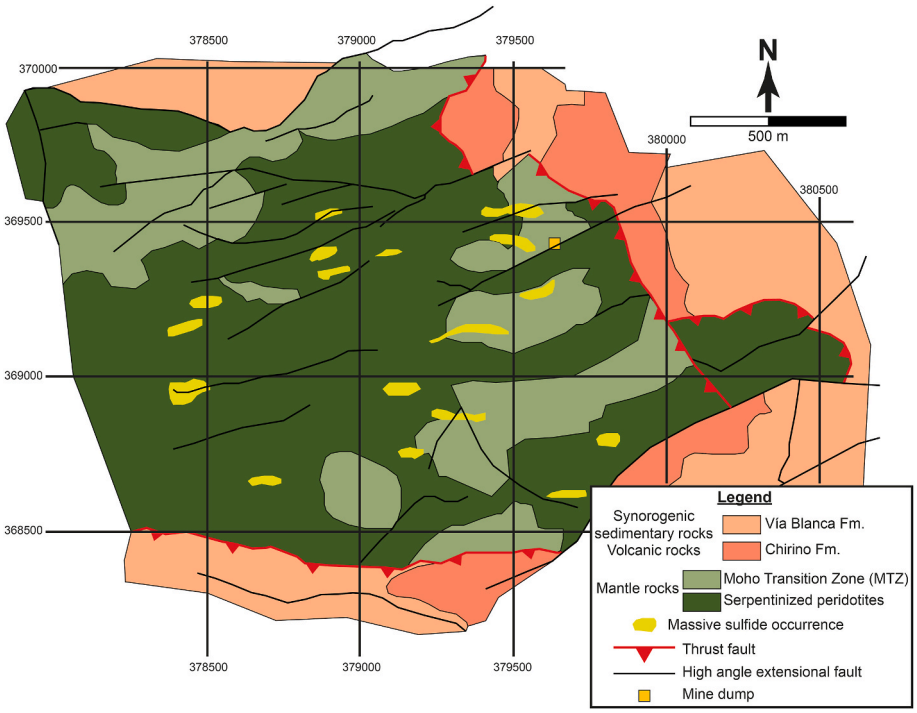

Fig. 3. Geological map of the Salomón mine (modified from Capote et al., 2006).

dunites from the MTZ (Genkin et al., 1990; Llanes et al., 2006).

The host peridotites are commonly characterized by heavy serpentinization, and Cr-spinel is the only remnant of the primary mantle mineral assemblage. Pervasive carbonatization and local chloritization and silicification are observed in the host serpentinized peridotites. The ore bodies are affected by oxidation, which triggered the development of secondary copper minerals such as azurite and malachite, and Fe oxy-hydroxides such as goethite and hematite (Fig. 2b–c, f). Importantly, the mineralization is largely restricted to tectonized areas and mostly associated with NE-SW and E-W trending shear faults (Genkin et al., 1990; Llanes et al., 2001, 2006).

3. Sample background and analytical techniques

We studied 21 polished thin sections representative of mineralization and host rocks from the Lomas de Majana and Salomón deposits. Lomas de Majana samples were taken from outcrops of massive sulfide bodies (Fig. 2a–c). Salomón ore samples were collected in the dumps resulting from the old mining activity (Fig. 2e–f). One massive sulfide ore sample from the Lomas de Majana (HAV-5; Fig. 2c) was crushed, sieved, and processed using the hydroseparation technique (HS Lab, Universitat de Barcelona; www.hslab-barcelona.com) to obtain heavy mineral concentrates. The resulting concentrates were mounted as polished monolayers on resin blocks (SimpliMet 1000) for subsequent mineralogical investigation.

Both the polished thin sections and monolayers have been studied by optical and electron microscopy. The electron microscopy study was carried out using a Quanta FEI XTE 325/D8395 scanning electron microscope (SEM) equipped with an INCA Energy 250 EDS microanalysis system and a JEOL JSM-7100 field-emission SEM at the Centers Científics i Tecnològics de la Universitat de Barcelona (CCiTUB). Operating conditions were 20 kV accelerating voltage.

Quantitative electron microprobe analyses (EMPA) on spinel (Cr-spinel and magnetite), sulfides, arsenides, sulfarsenides, and electrum were conducted at CCiTUB with a JEOL JXA-8230 equipment using wavelength-dispersive spectroscopy (WDS). The analytical conditions were 15–20 kV accelerating voltage, 10–20 nA beam current, 1–2 μm beam diameter, and 10–20 s counting time (peak and background) per element. Measurements and calibrations were performed using the following natural and synthetic standards: Cr-spinel (Cr, Al, Fe), periclase (Mg), rutile (Ti), metallic V (V), NiO (Ni) and rhodonite (Mn) for spinel and GaAs (As), ZnSe (Se), HgS (Hg), metallic Au (Au), sphalerite (Zn), chalcopyrite (Cu), metallic Sb (Sb), metallic Ag (Ag), pyrite (Fe, S), HgTe (Te), metallic Co (Co), metallic Ni (Ni), metallic Cd (Cd) and galena (Pb) for sulfides, arsenides, sulfarsenides and electrum. The Fe^{2+} and Fe^{3+} contents in spinel group minerals have been estimated by stoichiometry. The complete EMPA results, together with the detection limits for each element, are provided in Supplementary Appendices 1 to 8.

X-ray (XR) images shown in Fig. 6a–d (5796 × 8862 μm; 414 x 633 pixels; 14 μm/pixel) were obtained using a JEOL JXA-8230 equipment using wavelength-dispersive spectroscopy (WDS) at CCiTUB. The operating conditions were 288 nA and 20 kV with a focused electron beam and counting time of 30 ms/pixel. The XR maps were obtained by WDS for S (Kα), Cu (Kα), Ni (Kα), As (Lα), Fe (Kα), Mg (Kα), Si (Kα), Cr Kα), Co (Kα), and Al (Kα), and by EDS for O (Kα), Ca (Kα), Ti (Kα), Mn (K α), Na (Kα), K (Kα), V (Kα), Zn (Kα), Ag (Lα), Sb (Lα), Te (Lα), Pt (Mα), Au (Mα), Hg (Lα), Pb (Mα), and Bi (Mα). Under these experimental conditions, only background levels were detected for As and K–Bi in the scanned area. The XR images were processed with DWImager software (Torres-Roldán and Garcia-Casco, unpublished; see García-Casco, 2007). The images presented were expressed in counts (color code). In all images, voids, polish defects, and silicate mineral phases not considered for illustration are masked out, and the resulting color images were overlain onto a reference grey-scale base image having the same spatial resolution (pixels) calculated with the expression Σ[counts(i)·A(i)] (A = Atomic number, i = S, Cu, Ni, Cr, Co, Si, Fe, and Mg) that contains the basic textural information of the scanned area.

4. Results

4.1. Ultramafic host rocks

The mantle section of Havana-Matanzas Ophiolitic Massif is

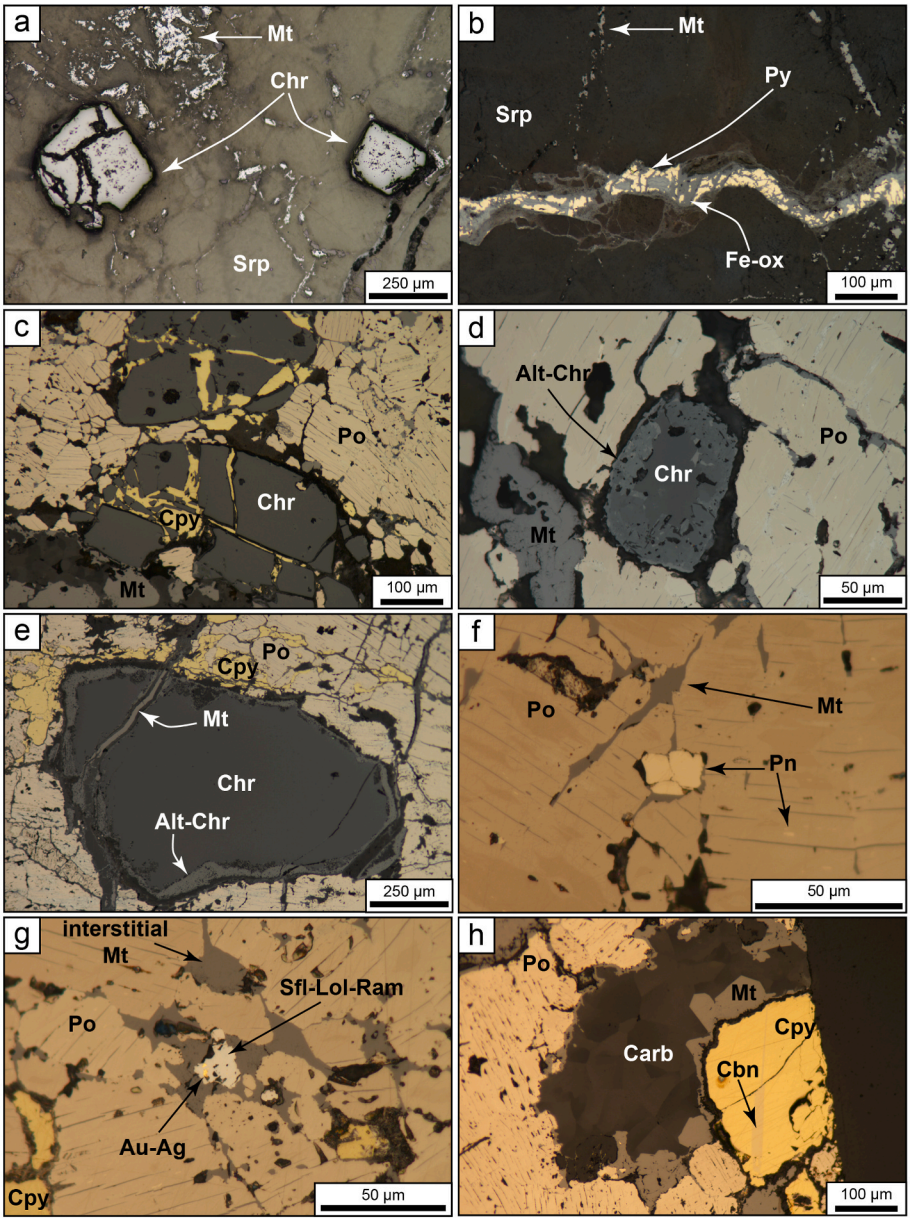

Fig. 4. Optical microscope pictures of a) subhedral Cr-spinel grains from the serpentinite host; b) Pyrite and Fe-oxide vein cutting the serpentinite; c) anhedral and fractured Cr-spinel grains. The fractures are filled with chalcopyrite; d) Cr-spinel grain with alteration rim of porous Cr-spinel; e) large grain of Cr-spinel with a thin rim of altered Cr-spinel crosscut by a late magnetite vein; f) pentlandite grain in an intergranular position with pyrrhotite; g) diarsenide grain from the safflorite-löllingite-rammelsbergite solid solution series with micro-inclusions of electrum; h) late pocket filled with magnetite and carbonates. Abbreviations: alt-chr: altered Cr-spinel, Au–Ag: electrum, carb: carbonates, cbn: cubanite, chr: Cr-spinel, cpy: chalcopyrite, Fe-ox: Fe-oxides, mt: magnetite, pn: pentlandite, po: pyrrhotite, py: pyrite, sfl-lol-ram: safflorite-löllingite-rammelsbergite, srp: serpentinite.

dominated by porphyroclastic harzburgites and dunites together with minor occurrences of peridotites impregnated with plagioclase and dikes of gabbro (Fig. 2d) and orthopyroxenite. Most of the ultramafic rocks are found within shear zones and therefore, they are deformed and brecciated. All these lithologies were substantially altered by hydration processes resulting in the transformation of most primary silicates (olivine + orthopyroxene ± clinopyroxene) into secondary minerals including serpentine-group minerals, chlorite, talc, and carbonates. These rocks have pseudomorphic mesh and hourglass textures showing bastitized orthopyroxenes up to 5 mm in size pseudomorphed by lizardite and minor chlorite, talc, and magnetite. Accessory Cr-spinel is the only primary mineral preserved in serpentinite. Cr-spinel grains are generally euhedral-subhedral (Fig. 4a) with sizes up to 0.5 mm. Back-scattered electron (BSE) images reveal that Cr-spinel grains have dark irregular cores surrounded by brighter and porous Cr-spinel and/or magnetite (Fig. 5a). These rocks also contain small disseminations and veinlets of sulfides, mostly pyrite, and Fe-oxides (Fig. 4b).

4.2. Ore mineralogy and petrography

All the studied ore samples from the Lomas de Majana and Salomón deposits have similar mineralogy and textures and are hence jointly described below.

Cr-spinel grains, ubiquitous in all massive sulfide samples, are generally rounded and show sizes ranging from 30 μm to 1 mm (Fig. 4c–e and Fig. 5b–d). Similar to Cr-spinel in the host ultramafic rocks, Cr-spinel in the ore samples usually shows dark irregular cores in BSE images surrounded by brighter and more porous rims (Fig. 4d–e and Fig. 5b–c). Porosity in rims is filled with silicate minerals, mostly chlorite. Finally, the grains are partially surrounded and replaced by a magnetite rim (Fig. 5b–c).

Massive sulfide samples have >90% modal proportion of sulfides. Cr-spinel, Fe-oxides, carbonates, and silicates complete the remaining 10% modal mineralogy. Among the sulfides, pyrrhotite (Figs. 4 and 5) is dominant (modal proportion >70%) and shows anhedral shapes and size up to 150 μm. Pyrrhotite grains are locally deformed, displaying folded cleavage suggestive of deformation related to shearing. Pentlandite is found as rounded grains 50 μm in size that occur interstitial to

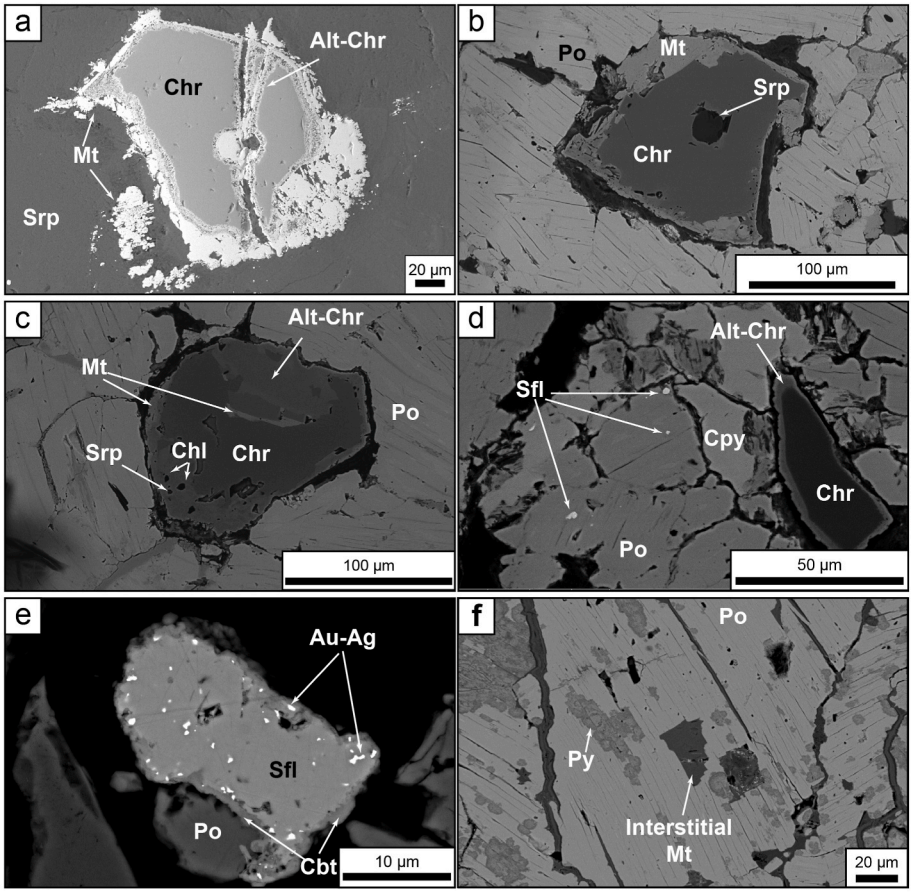

Fig. 5. BSE images of a) Cr-spinel grain with an altered Cr-spinel and magnetite halos from the serpentinite host; b) Cr-spinel grain with an inclusion of serpentine surrounded by a thin layer of altered Cr-spinel and a thick magnetite rim; c) Cr-spinel grain with large sectors of altered Cr-spinel. Some voids are filled with chlorite and serpentine; d) rounded safflorite grains included within pyrrhotite; e) safflorite grain in dense concentrate and including several electrum particles. Safflorite is rimmed by cobaltite; f) pyrite partially replacing pyrrhotite along its cleavage planes. Abbreviations: alt-chr: altered Cr-spinel, Au–Ag: electrum, cbt: cobaltite, chl: chlorite, chr: Cr-spinel, cpy: chalcopyrite, mt: magnetite, po: pyrrhotite, py: pyrite, sfl: safflorite, srp: serpentinite.

pyrrhotite grains, or as much smaller (<5 μm) inclusions within pyrrhotite (Fig. 4f). Diarsenides of the safflorite-löllingite-rammelsbergite series are found as ~30-μm crystals in an intergranular position with respect to other sulfides (Fig. 4g) but also as small inclusions (<5 μm) within pyrrhotite (Fig. 5d). In places, the contact between pyrrhotite and pentlandite/diarsenides is lined with interstitial magnetite. Rounded to droplet-like inclusions of Au–Ag up to ~30 μm in diameter occur in pyrrhotite. Au–Ag particles are also found as rounded micro-inclusions within the diarsenides (Figs. 4g and 5e). Bi–Te phases are scarce and only two grains have been identified along contacts between diarsenide and pyrrhotite. Chalcopyrite and cubanite (Fig. 4h) are anhedral and found in between pyrrhotite grains or filling fractures in Cr-spinel grains (Fig. 4c, e). Pyrite replaces pyrrhotite along cleavage planes (Fig. 5f), whereas sulfarsenides of the cobaltite-gersdorffite-arsenopyrite series partially replace diarsenide grains along grain boundaries (Fig. 5e).

Two different types of veins crosscut the massive sulfide assemblage. The first type is composed of serpentine and chlorite (Fig. 6) hosting remobilized, angular fragments of Au–Ag particles <5 μm in size. The second type is composed of magnetite (Fig. 6) and Ca–Fe–Mg carbonates with a wide compositional range (Fig. 6d).

Finally, supergene alteration of the primary sulfide mineralization has produced the formation of Fe-oxi-hydroxides such as goethite and hematite, and Cu-bearing carbonates such as malachite and azurite.

4.3. Mineral chemistry

4.3.1. Fe–Cu–Ni sulfides

Pyrrhotite (n = 63 analytical spots; Table 1) has variable Fe contents (55.7–64.4 wt%) and small but significant variations of Ni (from below detection limit [<D.L.] to 2.07 wt%), S (36.7–40.7 wt%), and Co (<D.L. – 0.29 wt%). The metal/sulfur ratio (M/S) varies between 0.82 and 0.99. Variation of Fe contents in pyrrhotite is well-defined in X-Ray maps (Fig. 6c), which highlight that some areas, especially around veins, are depleted in Fe. The structural formula for the analyzed pyrrhotite grains is $Fe_{0.82\text{-}0.99}S$.

Chalcopyrite grains (n = 19 analytical spots; Table 1) are almost stoichiometric with a formula varying from $(Fe_{1.03}Cu_{0.94})_{\sum=1.97}S_{2.03}$ to $(Fe_{0.98}Cu_{0.97}Co_{0.03})_{\sum=1.98}(S_{2.00}As_{0.02})_{\sum=2.02}$. Cobalt contents vary from <D.L. to 0.87 wt%.

The large crystals of pentlandite (≥20 μm) found in between pyrrhotite grains (n = 41 analytical spots; Table 1) are enriched in Co (11.7–14.6 wt%), and have a structural formula ranging from $(Fe_{4.03}Ni_{3.21}Co_{1.78}Cu_{0.01})_{\sum=9.03}S_{7.97}$ to $(Fe_{3.73}Ni_{3.30}Co_{1.87}Te_{0.01})_{\sum=8.92}S_{8.08}$ (Fig. 7).

4.3.2. Co–Ni–Fe diarsenides (safflorite-rammelsbergite-löllingite)

Analyzed diarsenide grains (n = 101 analytical spots; Table 2) have a slight variability in As (67.29–72.57 wt%) and low S contents (0.32–2.40 wt%). Cobalt (5.25–15.6 wt%), Fe (6.90–14.5 wt%), and Ni (2.54–13.0 wt%) contents are more variable (Fig. 8a). Their structural formula ranges from $(Co_{0.54}Fe_{0.41}Ni_{0.09})_{\sum=1.04}(As_{1.90}S_{0.04}Se_{0.02})_{\sum=1.96}$ to $(Co_{0.18}Fe_{0.41}Ni_{0.42})_{\sum=1.01}(As_{1.89}S_{0.06}Se_{0.04})_{\sum=1.99}$.

4.3.3. Co–Ni–Fe sulfarsenides (cobaltite-gersdorffite-arsenopyrite)

A total of 58 analytical spots (Table 2) have been carried out in different sulfarsenide grains (Fig. 8b). They present variable contents of Co (7.28–29.3 wt%), Fe (4.29–14.0 wt%), Ni (1.83–15.4 wt%), As (37.9–47.1 wt%), and S (14.0–22.9 wt%). The structural formula for the sulfarsenide grains varies from $(Co_{0.81}Fe_{0.13}Ni_{0.07})_{\sum=1.01}(S_{1.00}As_{0.98}Se_{0.01})_{\sum=1.99}$ to $(Co_{0.21}Fe_{0.35}Ni_{0.44})_{\sum=1.00}(S_{1.06}As_{0.93}Se_{0.01})_{\sum=2.00}$.

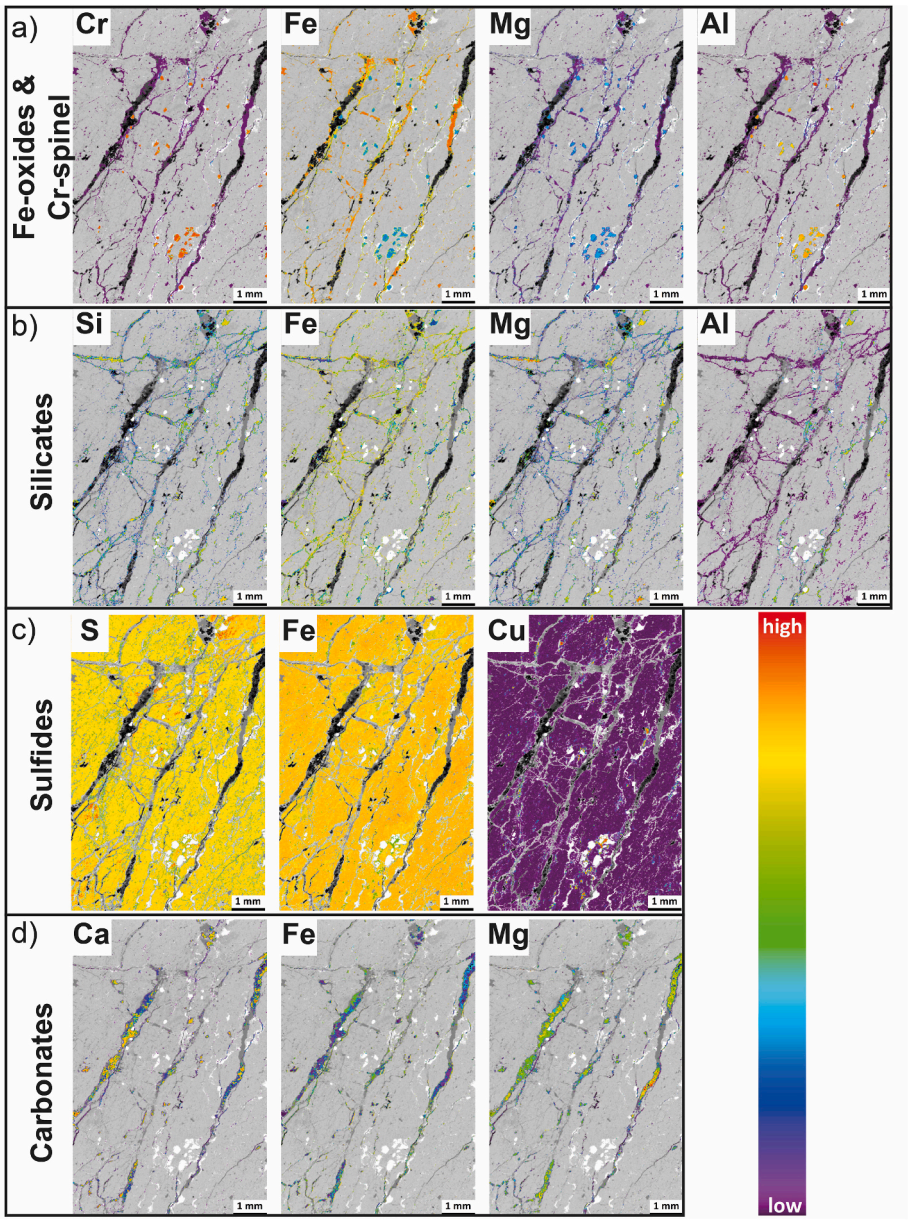

Fig. 6. X-ray images showing the textural and compositional features of a) Cr-spinel and Fe-oxides; b) hydrous silicates (mostly serpentine); c) sulfides; d) carbonates. The scales correspond to number of counts per pixel. The colored parts of the images correspond to minerals of interest that are set in a greyscale base-layer showing the basic textural feature of the scanned area (for clarity, see section 3 of the text).

4.3.4. *Electrum*

Analyzed Au–Ag particles included in pyrrhotite (n = 11 analytical spots; Table 3) have high Au (73.5–82.6 wt%) and lower Ag (15.7–24.1 wt%) contents and are classified as electrum. Low Fe contents have been detected in all analyses (0.11–0.85 wt%). The structural formula varies from $Au_{74}Ag_{26}$ to $Au_{61}Ag_{37}Fe_2$.

4.3.5. *Cr-spinel*

Dark cores of Cr-spinel (n = 93 analytical spots; Table 4) have Cr_2O_3 contents varying from 42.9 to 51.3 wt%, Al_2O_3 from 10.0 to 17.0 wt%, MgO from 6.90 to 11.8 wt%, and TiO_2 from 0.09 to 0.35 wt%. The Cr# [Cr/(Cr + Al) atomic ratio] ranges between 0.65 and 0.77, the Mg# [Mg/(Mg + Fe^{2+}) atomic ratio] varies between 0.36 and 0.57, and the Fe^{3+}# [Fe^{3+}/(Fe^{3+} + Cr + Al) atomic ratio] ranges between 0.01 and 0.13 (Fig. 9).

Brighter rims surrounding the dark cores of Cr-spinel grains (n = 21 analytical spots; Table 4) yield Cr_2O_3 values between 35.41 and 48.94 wt%, Al_2O_3 between 1.22 and 9.36 wt%, MgO between 2.08 and 6.45 wt %, and TiO_2 between 0.16 and 0.44 wt%. These contents correspond to higher Cr# (0.75–0.96) and Fe^{3+}# (0.15–0.36) and lower Mg# (0.11–0.34) relative to the unaltered cores (Fig. 10).

4.3.6. *Magnetite*

A total of 68 spot analyses (Table 5) show that magnetite in veins or in interstices exhibits higher Si (up to 0.16 a. p.f.u.) than the rims around Cr-spinel (up to 0.06 a. p.f.u.). The latter is also richer in Cr (up to 0.33 a. p.f.u.; Fig. 11).

5. Discussion

5.1. *Serpentinization processes prior and after the sulfide mineralization*

Cr-spinel grains in both the massive sulfide mineralization and serpentinized ultramafic rocks hosted in the studied UM-VMS from

Table 1
Representative EMPA data (wt. %) of sulfides from the Havana-Matanzas UM-VMS deposits (APFU = atoms per formula unit; b.d.l. = below detection limit).

Mineral	Pyrrhotite	Pyrrhotite	Pyrrhotite	Chalcopyrite	Chalcopyrite	Chalcopyrite	Pentlandite	Pentlandite	Pentlandite
Sample	HAV-5B	HAV-5C	HAV-5B	HAV-5B	HAV-5B	HAV-5B	HAV-5B	HAV-5B	HAV-5C
Analysis	2.18	1.1	2.19	4b.5	1.9	6.8	2.9	3.5	8.9
As	b.d.l.	b.d.l.	b.d.l.	b.d.l.	0.90	b.d.l.	b.d.l.	b.d.l.	b.d.l.
Se	b.d.l.	b.d.l.	b.d.l.	b.d.l.	b.d.l.	b.d.l.	b.d.l.	b.d.l.	b.d.l.
S	37.5	39.5	38.5	34.6	34.6	34.7	32.7	33.1	34.1
Pb	0.22	b.d.l.	b.d.l.	b.d.l.	b.d.l.	b.d.l.	b.d.l.	b.d.l.	b.d.l.
Sb	b.d.l.	b.d.l.	b.d.l.	b.d.l.	b.d.l.	b.d.l.	b.d.l.	b.d.l.	b.d.l.
Te	b.d.l.	b.d.l.	b.d.l.	b.d.l.	b.d.l.	b.d.l.	b.d.l.	b.d.l.	b.d.l.
Cu	b.d.l.	b.d.l.	b.d.l.	34.7	33.3	34.3	0.07	b.d.l.	b.d.l.
Ni	b.d.l.	0.22	b.d.l.	b.d.l.	0.11	b.d.l.	24.1	24.7	24.2
Co	0.07	0.09	b.d.l.	b.d.l.	0.87	b.d.l.	13.4	14.1	14.0
Fe	64.4	59.3	62.1	30.5	29.8	30.7	28.8	26.6	27.2
Total	102.24	99.05	100.54	99.81	99.83	99.69	99.07	98.78	99.75
APFU									
As	0.00	0.00	0.00	0.00	0.02	0.00	0.00	0.00	0.00
Se	0.00	0.00	0.00	0.00	0.00	0.00	0.00	0.00	0.00
S	1.00	1.00	1.00	1.99	1.99	1.99	7.96	8.08	8.21
Pb	0.00	0.00	0.00	0.00	0.00	0.00	0.00	0.00	0.01
Sb	0.00	0.00	0.00	0.00	0.00	0.00	0.00	0.00	0.00
Te	0.00	0.00	0.00	0.00	0.00	0.00	0.00	0.01	0.00
Cu	0.00	0.00	0.00	1.00	0.97	1.00	0.01	0.00	0.01
Ni	0.00	0.00	0.00	0.00	0.00	0.00	3.21	3.30	3.18
Co	0.00	0.00	0.00	0.00	0.03	0.00	1.78	1.87	1.83
Fe	0.99	0.86	0.93	1.01	0.98	1.01	4.03	3.73	3.76
Anions	1.00	1.00	1.00	1.99	2.02	1.99	7.96	8.08	8.22
Cations	0.99	0.87	0.93	2.01	1.98	2.01	9.04	8.92	8.78

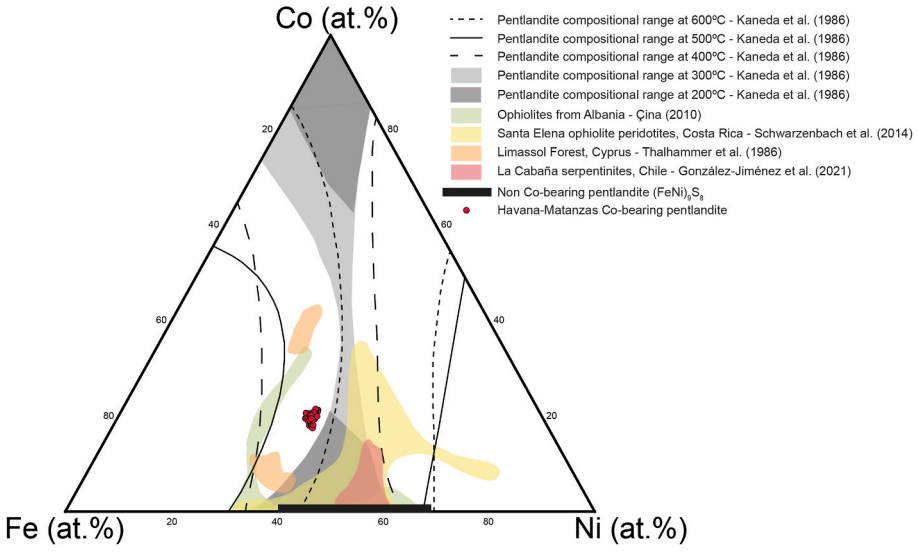

Fig. 7. Fe–Ni–Co ternary diagram for pentlandite (Çina, 2010; González-Jiménez et al., 2021; Schwarzenbach et al., 2014).

Havana-Matanzas exhibit dark irregular cores surrounded by brighter porous rims in BSE images.

The cores of Cr-spinel grains have low SiO_2 (average of 0.03 wt%) and Fe_2O_3 (average of 5.73 wt%) and high MgO (average of 9.94 wt%) and Al_2O_3 (average of 14.5 wt%) contents, similar to Cr-spinel compositions attributed by Proenza et al. (2004) to primary ophiolitic chromite. On the other hand, the brighter rims have high Fe_2O_3 (average of 16.6 wt%) and low MgO (average of 4.28 wt%) and Al_2O_3 (average of 4.95 wt%) contents. Thermodynamic modelling suggests that Cr-spinel becomes depleted in Al_2O_3 and MgO and proportionally enriched in Cr_2O_3 and FeO during serpentinization of mantle peridotites by hydrothermal fluids (Fig. 10; Kimball, 1990; Mellini et al., 2005; Gervilla et al., 2012). Cr-spinel alteration is accompanied by an increase in the porosity of the altered Cr-spinel, which is generally filled by chlorite (Gervilla et al., 2012). The alteration of Cr-spinel during serpentinization at T > 400 °C is described by the following reaction after Kimball (1990):

(Mg, Fe) $(Al,Cr)_2O_{4(Cr\text{-}spinel)}$+fluid → $Mg_5AlSi_3O_{10}(OH)_{8(chlorite)}$ + (Fe,Mg) $(Cr,Al)_2O_{4(alt.\ Cr\text{-}spinel)}$.

Consequently, the textural and chemical similarities of Cr-spinel grains hosted within the massive sulfide mineralization and serpentinized ultramafic rocks strongly suggest that at least the early stages of serpentinization occurred prior to the sulfide mineralization event.

The presence of Cr-spinel grains with homogeneous cores surrounded by irregular Fe^{2+}- and Fe^{3+}-rich alteration rims is expected in ocean floor serpentinization (Hajjar et al., 2022). Interestingly, Marques et al. (2007) concluded that the serpentinization associated with UM-VMS at Rainbow (Mid-Atlantic Ridge) took place before the mineralization event. Furthermore, Thalhammer et al. (1986) reported Cr-spinel grains with ferrian chromite and magnetite halos that preceded the sulfide mineralization at UM-VMS in Limassol Forest, Cyprus. Besides, serpentinization does not only precedes the formation of

Table 2
Representative EMPA data (wt.%) of arsenides from the Havana-Matanzas UM-VMS deposits (APFU = atoms per formula unit; b.d.l. = below detection limit).

Mineral	Diarsenide	Diarsenide	Diarsenide	Diarsenide	Diarsenide	Sulfarsenide	Sulfarsenide	Sulfarsenide	Sulfarsenide	Sulfarsenide
Sample	HAV5-53A	HAV5-53	HAV-5C	HAV5-30A	HAV5-30B	HAV-16-5	HAV-16-5	HAV-5-30B	HAV-5-53B	HAV-5-53A
Analysis	1.1	2.2	14e.5	6.2	7.4	1.15	1.5	6.2	1.1	4.3
As	70.5	70.7	70.2	70.1	70.4	44.5	45.2	45.6	43.4	45.1
Se	0.77	1.74	0.42	0.89	1.08	0.20	0.23	0.63	0.47	0.36
S	0.63	0.82	0.76	0.66	0.50	19.7	19.5	19.1	19.8	19.1
Pb	b.d.l.	b.d.l.	b.d.l.	b.d.l.	b.d.l.	b.d.l.	b.d.l.	b.d.l.	b.d.l.	b.d.l.
Sb	b.d.l.	0.20	b.d.l.	0.16	0.19	b.d.l.	b.d.l.	b.d.l.	b.d.l.	b.d.l.
Te	b.d.l.	b.d.l.	b.d.l.	b.d.l.	b.d.l.	b.d.l.	b.d.l.	b.d.l.	b.d.l.	b.d.l.
Cu	b.d.l.	b.d.l.	b.d.l.	b.d.l.	b.d.l.	b.d.l.	0.14	b.d.l.	b.d.l.	b.d.l.
Ni	2.54	12.3	7.89	9.07	10.6	2.80	3.64	13.4	14.7	4.09
Co	15.6	5.25	9.08	12.0	11.0	29.1	23.6	10.7	17.4	26.5
Fe	11.3	11.3	10.8	7.93	7.08	4.37	8.42	11.2	4.39	4.76
Total	101.28	102.24	99.09	100.76	100.80	100.65	100.68	100.61	100.19	99.90
APFU										
As	1.91	1.89	1.94	1.91	1.92	0.97	0.99	1.00	0.95	1.00
Se	0.02	0.04	0.01	0.02	0.03	0.00	0.00	0.01	0.01	0.01
S	0.04	0.05	0.05	0.04	0.03	1.01	1.00	0.98	1.01	0.99
Pb	0.00	0.00	0.00	0.00	0.00	0.00	0.00	0.00	0.00	0.00
Sb	0.00	0.00	0.00	0.00	0.00	0.00	0.00	0.00	0.00	0.00
Te	0.00	0.00	0.00	0.00	0.00	0.00	0.00	0.00	0.00	0.00
Cu	0.00	0.00	0.00	0.00	0.00	0.00	0.00	0.00	0.00	0.00
Ni	0.09	0.42	0.28	0.32	0.37	0.08	0.10	0.37	0.41	0.12
Co	0.54	0.18	0.32	0.42	0.38	0.81	0.66	0.30	0.48	0.75
Fe	0.41	0.41	0.40	0.29	0.26	0.13	0.25	0.33	0.13	0.14
Anions	1.97	1.99	2.00	1.97	1.98	1.98	1.99	1.99	1.98	1.99
Cations	1.03	1.01	1.00	1.03	1.02	1.02	1.01	1.01	1.02	1.01

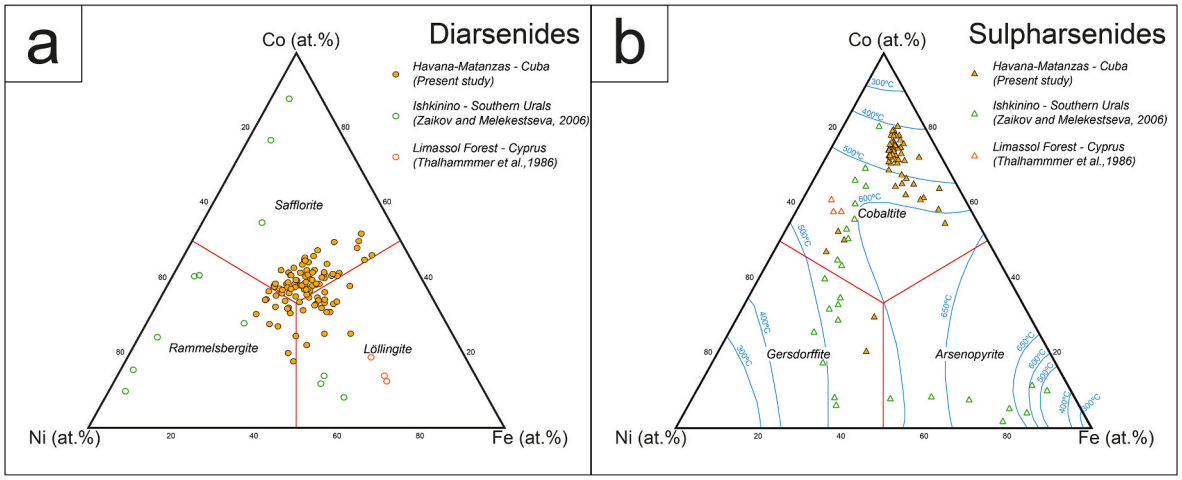

Fig. 8. Composition of a) diarsenides and b) sulfarsenides. Data from Ishkinino after Zaikov and Melekestseva (2006) and from Limassol Forest after Thalhammer et al. (1986). Isotherms in b) are after Klemm (1965).

UM-VMS, but also of other types of deposits such as the serpentine-hosted massive arsenide deposits at Bou Azzer, Morocco (Tourneur et al., 2021; Hajjar et al., 2022).

Late veins, filled with Mg–Fe silicates such as serpentine, Ca–Fe–Mg carbonates, and magnetite, crosscut the massive sulfide assemblage (Fig. 6). Similar late-stage mineralization has been described by several authors to indicate the wane of hydrothermal fluid circulation, which leads to Si–Ca–Mg–C metasomatism (e.g., Nimis et al., 2004; Bach et al., 2013; Alt et al., 2018; Coltat et al., 2019, 2021).

5.2. Mineralization stages

Based on field and textural relationships between the ore and gangue minerals (Figs. 4 and 5) we propose a five-stage paragenetic sequence for UM-VMS from the Havana-Matanzas ophiolites (Fig. 13):

1) Pre-ore stage: Unaltered Cr-spinel within the massive sulfide mineralization and within serpentinite hosts representing the primary mineralogy from the upper mantle peridotite (harzburgite-dunite) rock (Fig. 4a–e; Fig. 5a–d) was partially altered during the serpentinization process. Consequently, Cr-spinel developed porous, Fe^{2+}- and Fe^{3+}-rich rims (ferrian chromite; Fig. 10) filled with silicate inclusions (mostly chlorite). Later, they were partially surrounded and replaced by Cr-rich magnetite (Fig. 5a–c and Fig. 10). In parallel, the silicate mantle mineralogy underwent replacement by the hydrous silicate assemblage plus disseminated magnetite.
2) Ore stage I: Formation of the main sulfide mineral assemblage during the replacement of the serpentinized ultramafic rocks. This stage is dominated by pyrrhotite, a mineral indicative of reducing conditions. Such reducing conditions have been documented in several UM-SMS where the mineralizing hydrothermal fluids have been sampled, such as in Rainbow, Logatchev-1 and Ashadze deposits (Fouquet et al., 2010 and references therein). These reducing

Table 3
Representative EMPA data (wt.%) of electrum from the Havana-Matanzas UM-VMS deposits (APFU = atoms per formula unit; b.d.l. = below detection limit).

Sample	HAV-16-5	HAV-16-5	HAV-16-5	HAV-16-5	HAV-16-5	HAV-16-5
Analysis	2.1	2.2	3.1	3.3	3.6	3.7
Ag	18.1	15.7	20.2	20.0	23.7	24.1
Te	b.d.l.	b.d.l.	b.d.l.	b.d.l.	b.d.l.	b.d.l.
Cd	b.d.l.	b.d.l.	b.d.l.	b.d.l.	b.d.l.	b.d.l.
Au	80.8	82.6	78.5	78.4	75.3	73.5
Fe	0.77	0.22	0.56	0.58	0.85	0.85
Hg	b.d.l.	b.d.l.	b.d.l.	b.d.l.	b.d.l.	b.d.l.
Cu	b.d.l.	b.d.l.	b.d.l.	b.d.l.	b.d.l.	b.d.l.
Total	99.69	98.53	99.29	99.00	99.87	98.48
Atomic percentage						
Ag	28.30	25.65	31.32	31.19	35.53	36.45
Te	0.22	0.00	0.00	0.00	0.10	0.27
Cd	0.00	0.00	0.00	0.00	0.00	0.00
Au	69.16	73.67	66.68	67.05	61.79	60.77
Fe	2.31	0.68	1.66	1.76	2.46	2.49
Hg	0.00	0.00	0.33	0.00	0.00	0.00
Cu	0.00	0.00	0.00	0.00	0.12	0.03
Total	100.00	100.00	100.00	100.00	100.00	100.00

conditions were promoted by the ongoing multistage serpentinization as long as this process oxidizes the ferrous iron of olivine and pyroxene, thus favoring the formation of low-sulfur sulfide assemblages (Frost, 1985; Delacour et al., 2008; Klein and Bach, 2009; Evans et al., 2017). The assemblage in equilibrium with these reducing conditions falls within the pyrrhotite and löllingite (diarsenide) stability fields (Einaudi et al., 2005), thus promoting the crystallization of these phases together with Co-bearing pentlandite, chalcopyrite-cubanite, and electrum. According to experimental data (Kaneda et al., 1986), the analyzed Co-bearing pentlandite crystallized at temperatures ranging from 400 °C to 500 °C (Fig. 7). Such temperature range is similar to that measured at oceanic seafloor high-temperature (>400 °C) hydrothermal vents (Monecke et al., 2016 and references therein). The UM-VMS sulfide mineralization at Limassol Forest has also been estimated to be formed at temperatures between 400° and 500 °C (Thalhammer et al., 1986).

In some UM-SMS, such as Ashadze-1, Rainbow and Logatchev-1 (Mid-Atlantic Ridge), pyrrhotite is among the first sulfides to be deposited together with chalcopyrite-cubanite and minor amounts of gold, electrum, and Co-bearing sulfides from high temperature reduced fluids (Mozgova et al., 2008; Fouquet et al., 2010; Firstova et al., 2016). UM-VMS are often also characterized by a sulfide assemblages dominated by pyrrhotite and chalcopyrite, and minor amounts of Co-bearing pentlandite, diarsenides, and gold such as in the Urals (Zaikov and Melekestseva, 2006; Nimis et al., 2008) and Limassol Forest (Thalhammer et al., 1986).

3) Ore stage II: In this stage, pyrite replaces pyrrhotite whereas sulfarsenides partially replace diarsenide grains along their grain boundaries (Fig. 5e–f). These mineral replacements are the result of an increase in the fO_2 and fS_2 (Einaudi et al., 2005) during a more advanced serpentinization stage in which lesser amounts of olivine and pyroxene are available to be serpentinized (Delacour et al., 2008) and/or by an increase in the seawater component in the hydrothermal fluids (Hochscheid et al., 2022). This shift of replacement to a more sulfur-rich mineral assemblage, particularly the transformation of pyrrhotite into pyrite, has also been described in the UM-VMS from Limassol Forest (Thalhammer et al., 1986) and the Urals (Zaikov and Melekestseva, 2006; Nimis et al., 2008). A comparison of the analyzed sulfarsenides with experimental data in the Co–Fe–Ni–As–S system (Klemm, 1965) indicates that sulfarsenides were formed at temperatures between 400° and 500 °C (Fig. 8b), implying similar temperatures with ore stage I.
4) Late vein stage: Two different vein types crosscut the massive sulfides. One consists of Fe–Mg silicates (Fig. 6b), mostly serpentine-group minerals, whereas the other vein type is filled with carbonates, especially magnesite and dolomite, and magnetite (Fig. 6a, d). These vein types record the general wane of the hydrothermal system as described in other UM-VMS deposits (e.g. Nimis et al., 2004; Alt et al., 2018; Coltat et al., 2019, 2021).
5) Supergene alteration: Surface weathering of the primary sulfide mineralization has produced the formation of Fe-oxy-hydroxides such as hematite and goethite and Cu-bearing carbonates such as malachite and azurite.

5.3. Formation of the VMS mineralization in a fore-arc environment

As noted above, the cores of Cr-spinel grains occluded in pyrrhotite of the studied UM-VMS preserve their original mantle signature. Therefore, they can provide direct information on the geodynamic setting of formation of the peridotites and hosted UM-VMS (Kamenetsky

Table 4
Representative EMPA data (wt.%) of Cr-spinel from the Havana-Matanzas UM-VMS deposits (APFU = atoms per formula unit; b.d.l. = below detection limit).

Sample	HAV-5B	HAV-5B	HAV-5B	HAV-5B	HAV-5C	HAV-5B	HAV-5B	HAV-5B	HAV-5C	HAV-5C
Analysis	4.1	5.2	6.2	10.6	7.1	7.6	7.7	7.1	7.9	10.1.1
Core/Rim	Dark core	Dark core	Dark core	Dark core	Dark core	Bright rim	Bright rim	Bright rim	Bright rim	Bright rim
SiO_2	0.02	0.00	0.01	0.02	0.02	0.03	0.00	0.02	0.02	0.02
TiO_2	0.19	0.14	0.14	0.27	0.19	0.36	0.40	0.16	0.25	0.30
V_2O_5	0.24	0.32	0.29	0.27	0.24	0.46	0.56	0.24	0.26	0.25
Al_2O_3	15.0	15.5	15.0	12.0	13.9	6.66	5.41	5.88	6.15	1.95
Cr_2O_3	51.3	49.5	50.9	50.2	49.4	47.3	45.1	43.5	47.7	42.1
FeO_t	20.8	21.7	20.8	27.1	24.4	37.7	42.1	42.4	35.4	42.2
MnO	0.38	0.38	0.37	0.48	0.49	0.73	0.63	0.63	0.56	0.53
MgO	11.5	11.3	11.3	8.71	8.92	3.48	2.08	3.45	5.19	4.10
Total	99.36	98.71	98.75	99.00	97.50	96.78	96.28	96.29	95.50	91.45
APFU (4 oxygens)										
Cr	1.30	1.26	1.30	1.32	1.30	1.35	1.31	1.25	1.36	1.28
Ti	0.00	0.00	0.00	0.01	0.00	0.01	0.01	0.00	0.01	0.01
V	0.00	0.00	0.00	0.00	0.00	0.01	0.01	0.00	0.00	0.00
Al	0.57	0.59	0.57	0.47	0.55	0.28	0.23	0.25	0.26	0.09
Fe^{3+}	0.11	0.13	0.11	0.19	0.13	0.33	0.41	0.48	0.35	0.60
Fe^{2+}	0.44	0.46	0.45	0.56	0.55	0.81	0.88	0.80	0.71	0.76
Mn	0.01	0.01	0.01	0.01	0.01	0.02	0.02	0.02	0.02	0.02
Mg	0.55	0.54	0.54	0.43	0.44	0.19	0.11	0.19	0.28	0.24
Mg# = Mg/(Mg + Fe^{2+})	0.55	0.54	0.55	0.43	0.45	0.19	0.11	0.19	0.28	0.24
Cr# = Cr/(Cr + Al)	0.70	0.68	0.69	0.74	0.70	0.83	0.85	0.83	0.84	0.94
Fe^{3+}# = Fe^{3+}/(Fe^{3+}+Cr + Al)	0.06	0.07	0.06	0.10	0.07	0.17	0.21	0.24	0.18	0.31

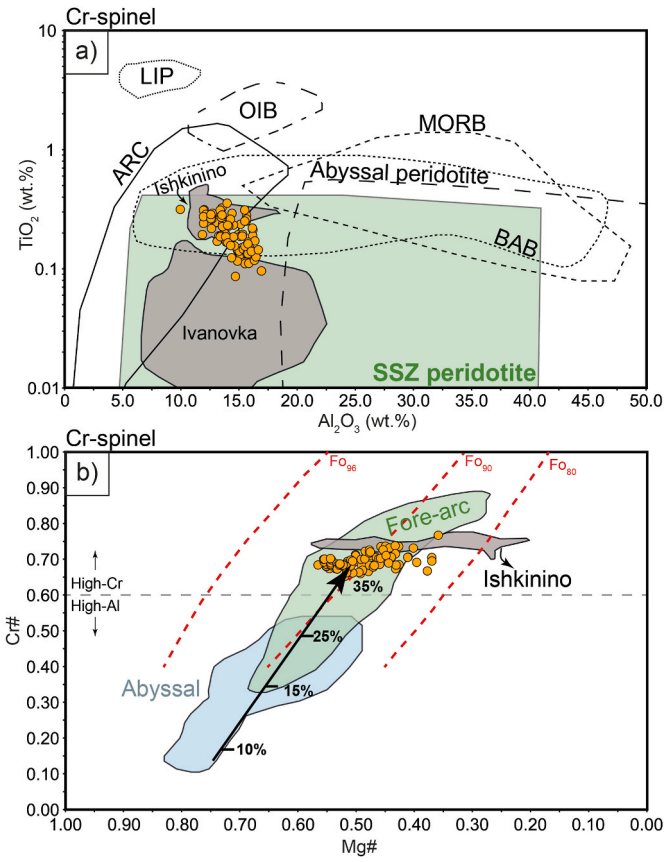

Fig. 9. Composition of unaltered Cr-spinel cores from within the massive sulfide lenses. a) Al_2O_3 (wt.%) vs TiO_2 (wt.%) diagram. Data from Ishkinino and Ivanovka is after Zaikov and Melekestseva (2006) and Nimis et al. (2008). Fields for LIP (Large Igneous Province), OIB (Ocean Island Basalt), Arc, MORB (Mid-Ocean Ridge Basalt), Abyssal peridotite, BAB (Back-Arc Basalt) and SSZ (Supra-subduction zone) are after Kamenetsky et al. (2001); b) Mg# vs Cr# diagram. Data from Ishkinino after Zaikov and Melekestseva (2006). Fields for fore-arc and abyssal peridotites are after Lian et al. (2016). Dashed lines represent the composition of olivine in equilibrium with Cr-spinel at 1200 °C after Dick and Bullen (1984).

et al., 2001; Pagé and Barnes, 2009). The composition of the primary Cr-spinel in the Havana-Matanzas mineralization corresponds to the SSZ type in the Al_2O_3 (wt.%) vs TiO_2 (wt.%) diagram in Fig. 9a. In the Mg# vs Cr# diagram, they plot within the fore-arc field and overlap the compositional range of Cr-spinel from the Ishkinino UM-VMS (Fig. 9b). These observations indicate that the Havana-Matanzas UM-VMS were formed in a SSZ environment, specifically in a fore-arc region. These compositions are equivalent to those reported as primary Cr-spinel in the ultramafic host rocks by Llanes-Castro (2016) and Proenza et al. (2016), which were considered by these authors as indicative of a subduction-related environment of formation. In addition, Cr-spinel compositions from orthopyroxenenite bands and high-Cr chromitites hosted in mantle section of the Havana-Matanzas peridotites indicate crystallization in equilibrium with boninitic melts (Farré-de-Pablo et al., 2020), thus supporting their contextualization in the fore arc environment (Nimis et al., 2008, 2010; Patten et al., 2022).

Table 5
Representative EMPA data (wt.%) of magnetite from the Havana-Matanzas UM-VMS deposits (APFU = atoms per formula unit; b.d.l. = below detection limit).

Sample	HAV-5B	HAV-5B	HAV-5C	HAV-5B	HAV-5B	HAV-5C
Analysis	7.8	8.5	11.9	7.1	11.7	7.2.6
Type	Rim	Rim	Rim	Vein/ Interstitial	Vein/ Interstitial	Vein/ Interstitial
Al_2O_3	0.31	b.d.l.	1.42	1.63	b.d.l.	b.d.l.
V_2O_5	b.d.l.	b.d.l.	0.12	b.d.l.	b.d.l.	b.d.l.
SiO_2	1.59	0.39	0.05	4.31	2.34	0.43
TiO_2	b.d.l.	b.d.l.	b.d.l.	b.d.l.	b.d.l.	b.d.l.
MnO	0.18	0.17	0.15	0.20	b.d.l.	0.11
Cr_2O_3	4.63	2.69	10.70	1.66	0.14	b.d.l.
MgO	1.50	0.74	0.12	4.92	2.05	0.26
FeO_t	86.1	89.7	80.0	79.7	86.9	90.4
Total	94.29	93.72	92.56	92.43	91.43	91.21
APFU (4 oxygens)						
Al	0.01	0.00	0.06	0.07	0.00	0.00
V	0.00	0.00	0.00	0.00	0.00	0.00
Si	0.06	0.01	0.00	0.16	0.09	0.02
Ti	0.00	0.00	0.00	0.00	0.00	0.00
Mn	0.00	0.00	0.00	0.00	0.00	0.00
Cr	0.14	0.08	0.33	0.05	0.00	0.00
Mg	0.08	0.04	0.01	0.27	0.12	0.02
Fe^{3+}	1.72	1.89	1.59	1.56	1.82	1.97
Fe^{2+}	0.97	0.97	1.00	0.89	0.97	1.00

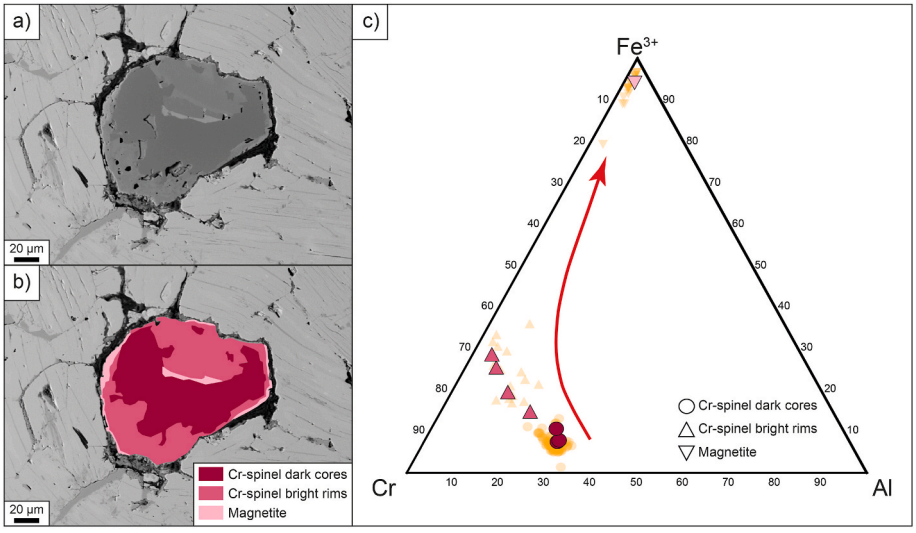

Fig. 10. a) BSE image of a Cr-spinel grain with an irregular dark core surrounded by a Cr-spinel bright rim and magnetite; b) Distinction of the three different zones within the grain in a); c) Composition of the Cr-spinel dark cores and bright rims and the magnetite rims in a Cr–Al–Fe^{3+} ternary diagram. The analyses shown in a-b) are highlighted in reddish colors (color legend as in b). The rest of the analyses are plotted in yellow.

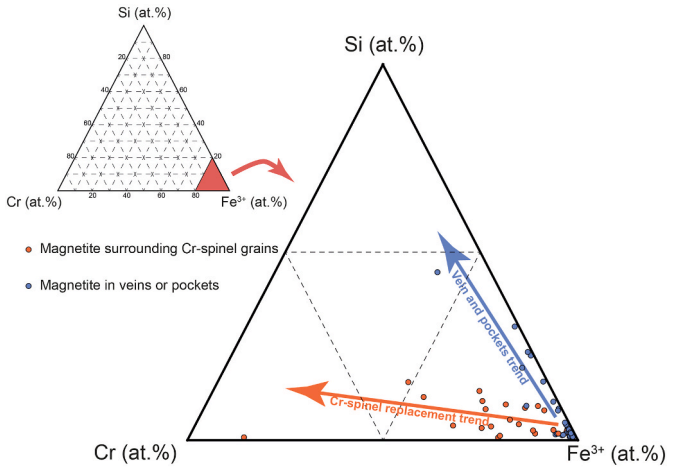

Fig. 11. Composition of magnetite surrounding Cr-spinel grains and magnetite located in veins or pockets in a Cr–Si–Fe^{3+} ternary diagram.

The geochemistry of volcanic rocks from Havana-Matanzas ophiolites also accords well with a SSZ environment. Basaltic rocks are classified as boninites, low-Ti island arc tholeiites (LOTI), 'normal' island arc tholeiites (IAT) and MORB-like basalts (compatible both with back-arc basin or fore-arc basalts; Fig. 12) (Llanes-Castro, 2016; Llanes et al., 2015b; Proenza et al., 2016). These geochemical signatures hence indicate formation of oceanic lithosphere in a fore-arc setting of an intra-oceanic arc, most probably during subduction initiation (Dilek and Furnes, 2011; Pearce, 2014; Shervais, 2022).

Arsenic enrichment of the studied UM-VMS, as evidenced by the conspicuous occurrence of Co–Ni–Fe diarsenide and sulfarsenide minerals, is a common feature in UM-VMS formed in SSZ environments (Patten et al., 2022). Arsenic is typically enriched in ultramafic rocks located in SSZ due to contamination derived from the subducting slab (Hattori and Guillot, 2003; Deschamps et al., 2013; Patten et al., 2017). It is also noteworthy that the compositions of diarsenides, sulfarsenides, and pentlandite from Ishkinino and Limassol Forest UM-VMS, both formed in a SSZ, are very similar to the same mineral phases analyzed here for Havana-Matanzas (Figs. 7 and 8).

Gold enrichment in UM-VMS deposits, such as it is the case of the studied deposits for which Au grades are up to 10 g/t, is a further indicator of UM-VMS deposits formed in SSZ setting compared to the Au-poorer UM-VMS formed in other geodynamic environments (Patten et al., 2022).

Early fore-arc environments are characterized by extension of the lithosphere during subduction initiation when the proto-trench retreats. In this environment, or in evolved stages of subduction affected by trench retreat, extension of the oceanic fore-arc takes place, triggering low-angle detachment faults that remove large parts of the crustal section of the lithosphere (e.g., Tremblay et al., 2009; Maffione et al., 2015; Morris et al., 2017), as seems to be case in the Havana-Matanzas ophiolite where the lower crustal sections are scarce or even not normally present in particular outcrops where the volcanic rocks of the upper crust occur in (tectonic) contact with the mantle (Fig. 1c and 14a).

5.4. Conceptual genetic model

The exhumation of the mantle peridotites (Fig. 14a) through low-angle detachment faults in oceanic extensional environments of slow spreading systems is considered to play an important role in the opening of pathways for fluid circulation (Cann et al., 2001; Escartín et al., 2008; Melekestseva et al., 2013; Elisha et al., 2014; Maffione et al., 2015; Morris et al., 2017). The onset of fluid circulation through the mantle rocks triggers partial serpentinization of the mantle mineralogy (olivine and pyroxene; Fig. 14b–c), including the alteration of Cr-spinel grains

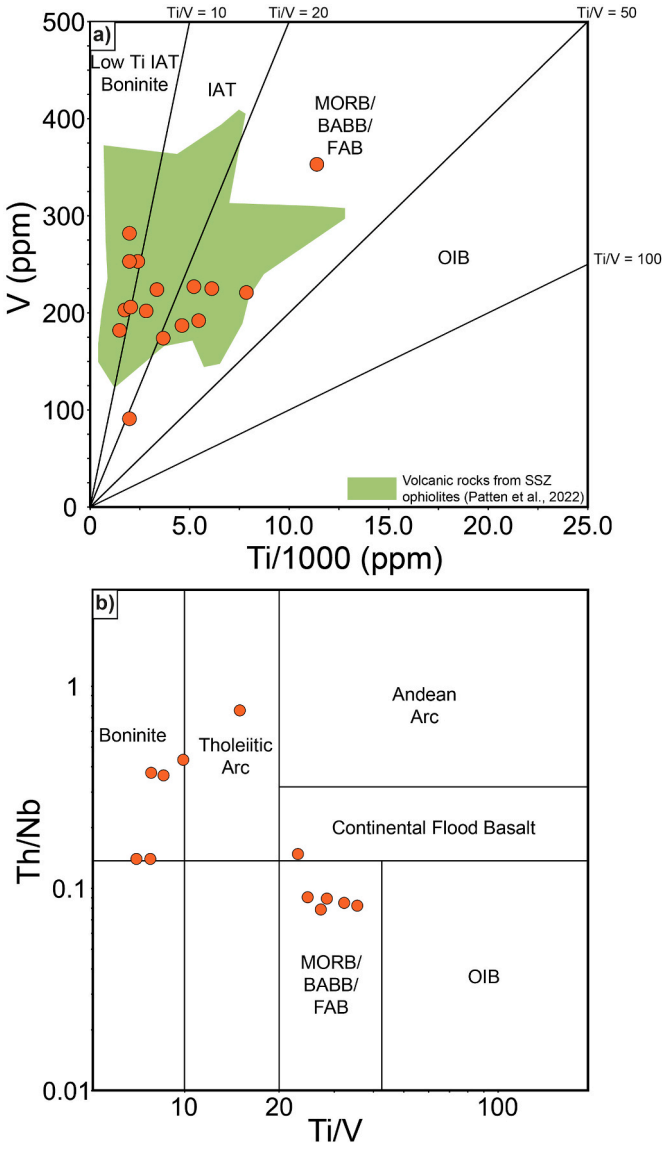

Fig. 12. Ti/1000 vs V, and Ti/V vs Th/Nb diagrams of basaltic volcanic rocks from the Havana-Matanzas ophiolitic massif. Data taken from Llanes-Castro (2016). Fields in a) from Shervais (1982) and Pearce (2008, 2014). Fields in b) are after Shervais (2022).

and the formation of Fe^{2+}-rich and Fe^{3+}-rich Cr-spinel first and magnetite after ongoing serpentinization (Fig. 14c). During the first stages of serpentinization, highly reducing conditions prevail due to oxidation of ferrous iron in olivine and pyroxene, a process that liberates H^+. (Frost, 1985; Delacour et al., 2008; Klein and Bach, 2009; Evans et al., 2017). Under low fO_2 and fS_2 conditions, hot (T > 400 °C) mineralizing fluids scavenge Fe, Co, Ni, and Au from the ultramafic host rocks (see Fouquet et al., 2010; Knight et al., 2018; Patten et al., 2022). These fluids are responsible for the replacement of the whole mineral assemblage of the partially serpentinized ultramafic rocks except for Cr-spinel grains. Such conditions favor the formation of a low-sulfur sulfide assemblage in which pyrrhotite is the most abundant mineral accompanied by Co-bearing pentlandite, diarsenides (mainly safflorite), chalcopyrite-cubanite and electrum (Fig. 14d). Pervasive replacement of the ultramafic lithologies by equivalent massive sulfide assemblages has been described in UM-SMS such as Rainbow (Marques et al., 2006, 2007) and in UM-VMS such as Ishkinino (Nimis et al., 2008) or Limassol Forest (Thalhammer et al., 1986). The multi-stage serpentinization process affecting the whole system would at some point consume most of

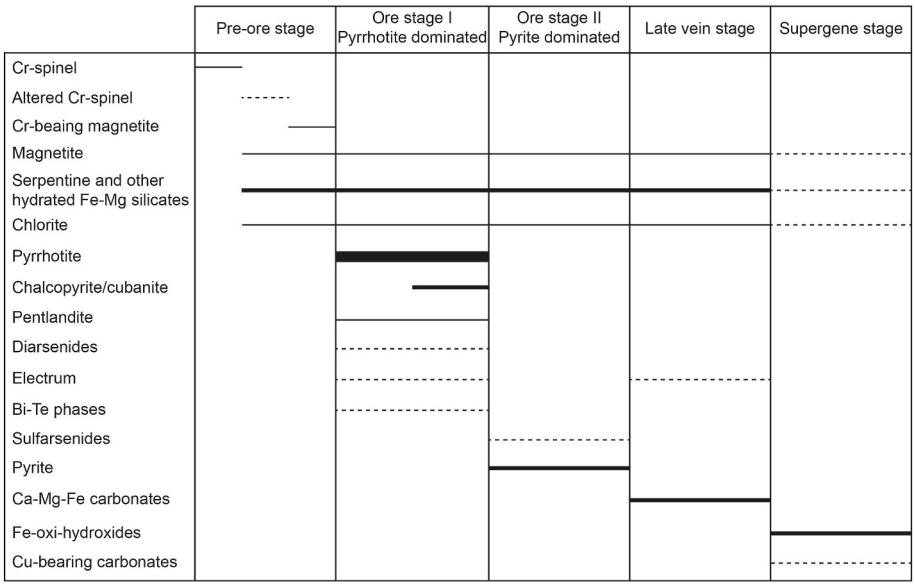

Fig. 13. Paragenetic sequence of the Havana-Matanzas UM-VMS deposits.

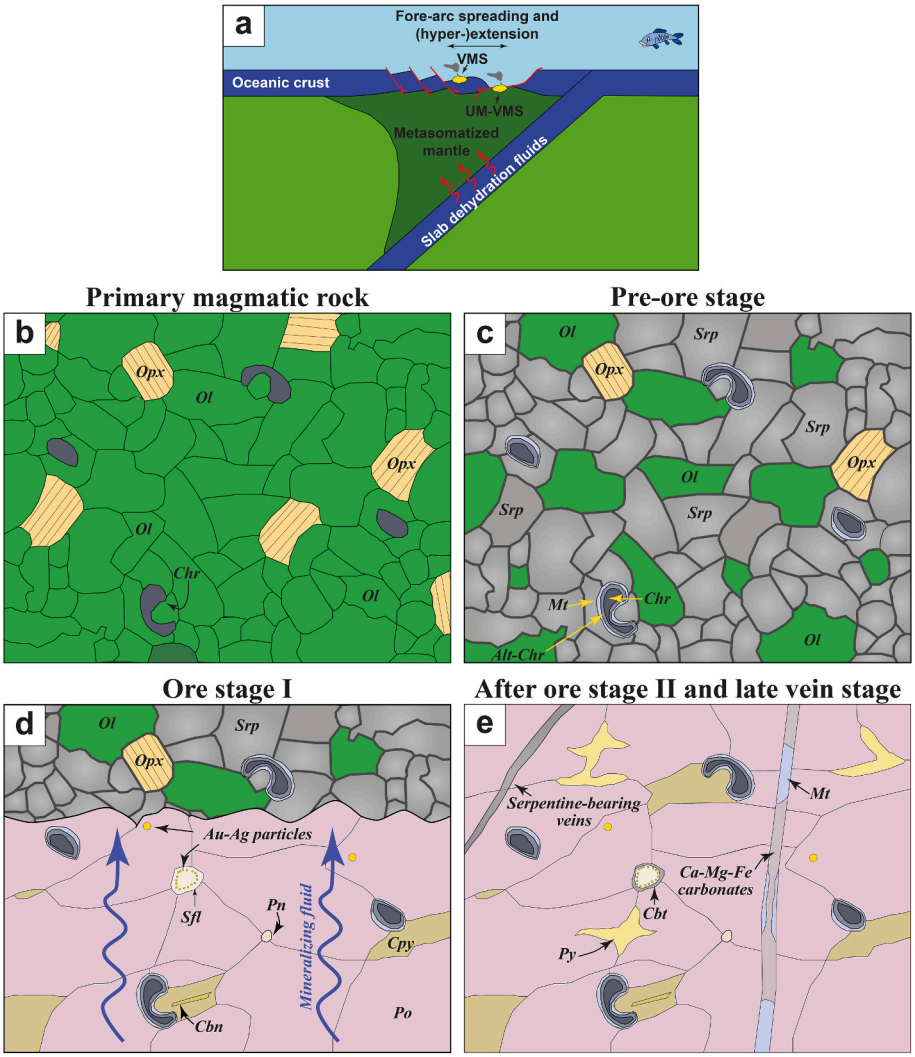

Fig. 14. Genetic model of formation of UM-VMS deposits from Havana-Matanzas. a) Formation of the deposits within the fore-arc region (general scheme modified from Patten et al., 2022); b) original protolith corresponding to a mantle harzburgite; c) exhumation of the mantle triggers the formation of large convection cells of hydrothermal fluid that partially serpentinize the mantle rocks; d) precipitation and replacement of the serpentinite by sulfides from the ore stage-I; e) increase of the of fS_2 and fO_2 produces the partial replacement of pyrrhotite and diarsenides by pyrite and sulfarsenides; late-stage serpentine and magnetite-carbonate veins crosscut the massive sulfide mineral assemblage. Abbreviations: alt-chr: altered Cr-spinel, Au–Ag: electrum, cbn: cubanite, cbt: cobaltite, chr: Cr-spinel, cpy: chalcopyrite, mt: magnetite, pn: pentlandite, ol: olivine, opx: orthopyroxene, po: pyrrhotite, py: pyrite, sfl: safflorite, srp: serpentinite.

the olivine and pyroxene, therefore producing a shift towards increasing fO_2 and fS_2 conditions in which pyrrhotite and diarsenides are unstable (Einaudi et al., 2005) and partially replaced by pyrite and sulfarsenides (mainly cobaltite). Increasing fO_2 and fS_2 could have also been favored by fluids with a larger seawater component, as suggested by Hochscheid et al. (2022). Finally, the wane of the circulation of progressively cooler hydrothermal fluids would be associated with the formation of late veins filled with Fe–Mg silicates, Ca–Fe–Mg carbonates, and magnetite crosscutting the whole massive sulfide mineralization (Fig. 14e).

5.5. Implications for exploration: UM-VMS deposits in Cuban ophiolites

According to Patten et al. (2022), UM-VMS deposits represent potential untapped mineral resources. In their review, these authors emphasize that, many on-land UM-VMS are found in SSZ ophiolites. Hence, exploring ultramafic units formed in SSZ environments is essential for targeting new UM-VMS deposits. In Cuba, the largest bodies of serpentinized peridotites and serpentinites crop out along the so-called Northern Cuban Ophiolite Belt and the Eastern Cuban Ophiolites (Iturralde-Vinent, 1996; Lewis et al., 2006; Iturralde-Vinent et al., 2016). These ophiolites consist of a >1000-km-long discontinuous belt with growing evidence of formation in a SSZ environment (Iturralde--Vinent et al., 2016; Proenza et al., 1999, 2016; Marchesi et al., 2006).

Greenfield exploration in the Cuban ophiolites for UM-VMS deposits must be accompanied by thorough geochemical characterization of the serpentinized peridotites and associated rocks, especially in areas close to tectonic contacts such as faults or shear zones that might have favored the circulation of hydrothermal fluids. Systematically, ultramafic host rocks close to the mineralization are intensely brecciated, sheared and serpentinized (>90%), and are spatially associated to carbonates, talc and quartz. Parts of the "Penrose" ophiolitic sequence (typically, large parts of the crustal section) in these areas would have generally been tectonically omitted due to the effects of extensional low-angle faults that may ultimately form oceanic core-complexes where mantle rocks approach the sea floor or are even exposed at the surface. The use of key pathfinder elements to the mineralization (e.g., As, Co, Ni) are crucial to plan adequate and strategic lithogeochemical campaigns. Detailed geophysical surveys are also critical. For example, magnetic surveys around the Lomas de Majana, Elena, and Caridad deposits (Fig. 1b) yielded positive magnetic anomalies around the mineralized ore bodies due to the magnetic properties of pyrrhotite (Llanes-Castro, 2016). Furthermore, shallow deposits that contain significant amounts of pyrrhotite and/or magnetite can be detected by electromagnetic, electrical or gravimetrical geophysical methods (Shanks and Thurston, 2012).

Therefore, geophysical surveys conducted in SSZ ophiolites can help delimiting possible areas of interest. Subsequently, in combination with the field and geochemical observations listed above, this exploration tool set could lead to the discovery of the next group of Cuban UM-VMS deposit.

6. Concluding remarks

The Havana-Matanzas UM-VMS formed in a supra-subduction zone environment, most probably in the fore-arc region during the initial stages of subduction and in a tectonic environment dominated by extension and low-angle normal faulting. These deposits were developed by the complete replacement of serpentinized ultramafic rocks beneath the seafloor. The sulfide mineralization was produced concomitant with the serpentinization process. The first ore stage was dominated by pyrrhotite and lesser amounts of Co-pentlandite, diarsenides, chalcopyrite-cubanite and electrum. This low-sulfidation assemblage precipitated from a very reducing hydrothermal fluid. The second and final ore stage is characterized by the partial replacement of pyrrhotite and diarsenides by pyrite and sulfarsenides, respectively, due to an increase in the of fS_2 and fO_2.

Declaration of competing interest

The authors declare that they have no known competing financial interests or personal relationships that could have appeared to influence the work reported in this paper.

Data availability

All used data can be found in the tables and supplementary appendixes of the paper.

Acknowledgements

This research was financially supported by Grant PID 2019-105625RB-C21 funded by MCIN/AEI/10.13039/501100011033. Additional funding was provided by a "Ayudas predoctorales 2020" number PRE 2020-092140 PhD grant to DD-C by the Spanish Ministry of Science and Innovation. LT acknowledges financial support from the CAP Investigación PUCP-2022 Program under grant agreement no. 2022-A-0047 [PI0975]. We greatly acknowledge the support given by Dr. Xavier Llovet from the Centers Científics i Tecnològics of the Universitat de Barcelona (CCiTUB) for his help with the EMPA. Reviewers Carl Nelson and Clifford Patten are deeply acknowledged for their constructive criticism and their very useful comments, which have helped to greatly improve the quality of the present manuscript.

Appendix A. Supplementary data

Supplementary data to this article can be found online at https://doi.org/10.1016/j.jsames.2022.103991.

References

Abdullin, A.A., Aniptov, I.A., Septov, N.S., 1999. Allochthon displaced mineral deposits and their occurrence (in Russian). Geol. Kazakhstan 2, 4–28.
Alt, J., Crispini, L., Gaggero, L., Levine, D., Lavagnino, G., Shanks, P., Gulbransen, C., 2018. Normal faulting and evolution of fluid discharge in a Jurassic seafloor ultramafic-hosted hydrothermal system. Geology 46, 523–526.
Bach, W., Jons, N., Klein, F., 2013. Metasomatism within the ocean crust. In: Metasomatism and the Chemical Transformation of Rock. Springer, pp. 253–288.
Brönniman, P., Rigassi, D., 1963. Contribution to the geology and paleontology of the area of the city of La Habana, Cuba, and its surroundings. Ecologae Geolicae Helvetica 56 (1), 193–430.
Cann, J.R., Prichard, H.M., Malpas, J.G., Xenophontos, C., 2001. Oceanic inside corner detachments of the Limassol forest área, troodos ophiolite, Cyprus. *10.1144/0016-764900-143* J. Geol. Soc. 158, 757–767.
Capote, C., Llanes, A.I., de la Nuez, D., 2006. Mapa geoestructural y de favorabilidad del sector Salomón, Provincia Habana, escala 1:5000. Unpublishe, Instituto de Geología y Paleontología, La Habana, Cuba.
Cazañas, X., Alfonso, P., Melgarejo, J.C., Proenza, J.A., Fallick, A.E., 2008. Geology, fluid inclusion and sulphur isotope characteristics of the El Cobre VHMS deposit, Southern Cuba. Miner. Deposita 43, 805–824.
Cazanas, X., Torres-Zafra, J.L., Lavaut-Copa, W., Cobiella-Reguera, J.L., Capote, C., González, V., López-Kramer, J.L., Bravo, F., Llanes, A.I., González, D., Ríos, Y., Ortega, Y., Yasmany, R., Correa, A., Pantaleón, G., Torres, M., Figueroa, D., Martin, D., Rivada, R., Núnez, A., 2017. Mapa Metalogénico de la República de Cuba a escala 1:250 000. Instituto de Geología y Paleontologia, Centro Nacional de Información Geológica, p. 95.
Çina, A., 2010. Pentlandite mineralization related to Albanian ophiolites. Scientific annals, school of geology, aristotle university of thessaloniki. Proceedings of the XIX CBGA congress thessaloniki, Greece. Special Volume 100, 317–323.
Coltat, R., Branquet, Y., Gautier, P., Campos Rodriguez, H., Poujol, M., Pelleter, E., McClenaghan, S., Manatschal, G., Boulvais, P., 2019. Unravelling the root zone of ultramafic-hosted black smokers-like hydrothermalism from an Alpine analog. Terra. Nova 31, 549–561. https://doi.org/10.1111/ter.12427.
Coltat, R., Boulvais, P., Riegler, T., Pelleter, E., Branquet, Y., 2021. Element distribution in the root zone of ultramafic-hosted black smoker-like systems: constraints from an Alpine analog. Chem. Geol. 559, 119916 https://doi.org/10.1016/j.chemgeo.2020.119916.
Delacour, A., Früh-Green, G.L., Bernasconi, S.M., 2008. Sulfur mineralogy and geochemistry of serpentinites and gabbros of the Atlantis Massif (IODP Site U1309). Geochem. Cosmochim. Acta 72, 5111–5127. https://doi.org/10.1016/j.gca.2008.07.018.
Deschamps, F., Godard, M., Guillot, S., Hattori, K., 2013. Geochemistry of subduction zone serpentinites: a review. Lithos 178, 96–127. https://doi.org/10.1016/j.lithos.2013.05.019.

Díaz-Martínez, R., 2010. La pequeña minería del oro en Cuba: historia, metalogenia y perspectiva. Bol. Soc. Geol. Mex. 62 (1), 187–198. https://doi.org/10.18268/BSGM2010v62n1a11.

Dick, H.J.B., Bullen, T., 1984. Chromian spinel as a petrogenetic indicator in abyssal and alpine-type peridotites and spatially associated lavas. *https://doi.org/10.1007/BF00373711.* Contrib. Mineral. Petrol. 86, 54–76.

Dilek, Y., Furnes, H., 2011. Ophiolite genesis and global tectonics: geochemical and tectonic fingerprinting of ancient oceanic lithosphere. GSA Bulletin 123, 387–411. https://doi.org/10.1130/B30446.1.

Ding, T., Tao, C., Dias, A.A., Liang, J., Chen, J., Wu, B., Ma, D., Zhang, R., Wang, J., Liao, S., 2021. Sulfur isotopic compositions of sulfides along the Southwest Indian Ridge: implications for mineralization in ultramafic rocks. Miner. Deposita 56, 991–1006. https://doi.org/10.1007/s00126-020-01025-0.

Einaudi, M.T., Hedenquist, J.W., Esra Inn, E., 2005. Sulfidation state of fluids in active and extinct hydrothermal systems: transitions simmons. In: S, F., Graham, I. (Eds.), Volcanic, Geothermal, and Ore-Forming Fluids: Rulers and Witnesses of Processes within the Earth. Special Publications of The Society of Economic Geologists, pp. 285–314. https://doi.org/10.5382/SP.10.15.

Elisha, B., Katzir, Y., Abelson, M., Agostini, S., Valley, J.W., Spicuzza, M.J., 2014. Fossil oceanic core complex in the Limassol Forest, Troodos ophiolite, Cyprus. In: International Symposium on Eastern Mediterranean Geology.

Escartín, J., Smith, D.K., Cann, J., Shouten, H., Langmuir, C.H., Escrig, S., 2008. Central role of detachment faults in accretion of slow spreading oceanic lithosphere. Nature 455, 790–794. https://doi.org/10.1038/nature07333.

Evans, K.A., Reddy, S.W., Tomkins, A.G., Crossley, R.J., Frost, B.R., 2017. Effects of geodynamic setting on the redox state of fluids released by subducted mantle lithosphere. Lithos 278–281, 26–42. https://doi.org/10.1016/j.lithos.2016.12.023.

Farré-de-Pablo, J., Pujol-Solà, N., Torres-Herrera, H., Aiglsperger, T., González-Jiménez, J.M., Llanes-Castro, A.I., Garcia-Casco, A., Proenza, J.A., 2020. Orthopyroxenite hosted chromitite veins anomalously enriched in platinum-group minerals from the Havana-Matanzas Ophiolite, Cuba. Bol. Soc. Geol. Mex. 72 (3), 2083–2102. https://doi.org/10.18268/BSGM2020v72n3a110620.

Firstova, A., Stepanova, T., Cherkashov, G., Goncharov, A., Babaeva, S., 2016. Composition and formation of gabbro-peridotite hosted seafloor massive sulfide deposits from the ashadze-1 hydrothermal field, mid-Atlantic Ridge. Minerals 6 (1), 19. https://doi.org/10.3390/min6010019.

Fonseca, E., Zelepugin, V.N., Heredia, M., 1985. Structure of the ophiolite association of Cuba. Geotectonics 1, 321–329.

Fouquet, Y., Cambon, P., Etoubleau, J., Charlou, J.L., Ondréas, H., Barriga, F., Cherkashov, G., Semkova, T., Poroshina, I., Bohn, M., Donval, J.P., Henry, K., Murphy, P., Rouxel, O., 2010. Geodiversity of hydrothermal processes along the Mid-Atlantic Ridge and ultramafic-hosted mineralization: a new type of oceanic Cu-Zn-Co-Au volcanogenic massive sulfide deposit. In: Rona, P.A., et al. (Eds.), Diversity of Hydrothermal Systems on Slow Spreading Ocean Ridges, vol. 188. AGU, pp. 321–367. https://doi.org/10.1029/2008GM000746.

Frost, B.R., 1985. On the stability of sulfides, oxides, and native metals in serpentinite. J. Petrol. 26, 31–63.

García-Casco, A., 2007. Magmatic paragonite in trondhjemites from the Sierra del Convento mélange, Cuba. Am. Mineral. 92, 1232–1237. https://doi.org/10.2138/am.2007.2598.

García-Casco, A., Iturralde-Vinent, M.A., Pindell, J., 2008. Latest cretaceous collision/accretion between the caribbean plate and caribeana: origin of metamorphic terranes in the greater Antilles. Int. Geol. Rev. 50, 781–809. https://doi.org/10.2747/0020-6814.50.9.781.

Garcia-Casco, A., Torres-Roldán, R.L., Iturralde-Vinent, M.A., Millán, G., Núñez Cambra, K., Lázaro, C., Rodríguez Vega, A., 2006. High pressure metamorphism of ophiolites in Cuba. Geol. Acta 4 (1–2), 63–88.

Genkin, A.D., Morales, A.R., Bortnikov, N.S., Kramer, J.L., Muraviskaya, G.N., 1990. Características de la mineralización aurífera en la mina Salomón. Provincia de La Habana, Unpublished, p. 21p.

Gervilla, F., Padrón-Navarta, J.A., Kerestedjian, T., Sergeeva, I., González-Jiménez, J.M., Fanlo, I., 2012. Formation of ferian Cr-spinel in podiform chromitites from the Golyamo Kamenyane serpentinite, Eastern Rhodopes, SE Bulgaria: a two-stage process. Contrib. Mineral. Petrol. 164, 643–657. https://doi.org/10.1007/s00410-012-0763-3.

González-Jiménez, J.M., Piña, R., Saunders, J.E., Plissart, G., Marchesi, C., Padrón-Navarta, J.A., Ramón-Fernández, M., Garrido, L.N.F., Gervilla, F., 2021. Trace element fingerprints of Ni–Fe–S–As minerals in subduction channel serpentinites. Lithos 400–401, 106432. https://doi.org/10.1016/j.lithos.2021.106432.

Hajjar, Z., Ares, G., Fanlo, I., Gervilla, F., González-Jiménez, J.M., 2022. Cr-spinel tracks genesis of Co-Fe ores by serpentinite replacement at Bou Azzer, Morocco. J. Afr. Earth Sci. 188, 104471 https://doi.org/10.1016/j.jafrearsci.2022.104471.

Hattori, K.H., Guillot, S., 2003. Volcanic fronts as a consequence of serpentinite dehydration in the mantle wedge. Geology 31, 525–528. https://doi.org/10.1130/0091-7613(2003)031<0525:VFFAAC>2.0.CO;2.

Haupert, I., Manatschal, G., Decarlis, A., Unternehr, P., 2016. Upper-plate magma-poor rifted margins: stratigraphic architecture and structural evolution. Mar. Petrol. Geol. 69, 241–261. https://doi.org/10.1016/j.marpetgeo.2015.10.020.

Hochscheid, F., Coltat, R., Ulrich, M., Munoz, M., Manatschal, G., Boulvais, P., 2022. The Sr isotope geochemistry of oceanic ultramafic-hosted mineralizations. Ore Geol. Rev. 144, 104824 https://doi.org/10.1016/j.oregeorev.2022.104824.

Iturralde-Vinent, M.A., 1996. Geología de las ofiolitas de Cuba. In: Iturralde-Vinent, M.A. (Ed.), Ofiolitas y arcos volcánicos de Cuba, IGCP Project 364, Special Contribution 1, 83–120.

Iturralde-Vinent, M.A., 1998. Sinopsis de la Constitución Geológica de Cuba. Acta Geol. Hisp. 33, 9–56.

Iturralde-Vinent, M.A., 2021. Geología de las mélange serpentíniticas de Cuba. En: Compendio de Geología de Cuba y del Caribe. Segunda Edición. (publicado Diciembre 2012), DVD-ROM. Editorial CITMATEL, 9-789592-572863.

Iturralde-Vinent, M.A., Díaz-Otero, C., García-Casco, A., Van Hinsbergen, D.J.J., 2008. Paleogene foredeep basin deposits of North-Central Cuba: a record of arc continent collision between the caribbean and North American plates. Int. Geol. Rev. 50, 863–884. https://doi.org/10.2747/0020-6814.50.10.863.

Iturralde-Vinent, M.A., Garcia-Casco, A., Rojas-Agramonte, Y., Proenza, J.A., Murphy, J. B., Stern, R.J., 2016. The geology of Cuba: a brief overview and synthesis. GSA Today (Geol. Soc. Am.) 26, 4–10. https://doi.org/10.1130/GSATG296A.1.

Kamenetsky, V.S., Crawford, A.J., Meffre, S., 2001. Factors controlling chemistry of magmatic spinel: an empirical study of associated olivine, Cr-spinel and melt inclusions from primitive rocks. J. Petrol. 42, 655–671. https://doi.org/10.1093/petrology/42.4.655.

Kaneda, H., Takenouchi, S., Shoji, T., 1986. Stability of pentlandite in the Fe–Ni–Co–S system. Miner. Deposita 21, 169–180.

Kerr, A.C., Iturralde-Vinent, M.A., Saunders, A.D., Babbs, T.L., Tarney, J., 1999. A new plate tectonic model of the Caribbean: implications from a geochemical reconnaissance of Cuban Mesozoic volcanic rocks. GSA Bulletin 111, 1581–1599. https://doi.org/10.1130/0016-7606(1999)111<1581:ANPTMO>2.3.CO;2.

Kimball, K.L., 1990. Effects of hydrothermal alteration on thecomposition of chromian spinels. Contrib. Mineral. Petrol. 105, 337–346.

Klein, F., Bach, W., 2009. Fe- Ni-Co-O-S phase relations in peridotite-seawater interactions. J. Petrol. 50 (1), 37–59. https://doi.org/10.1093/petrology/egn071.

Klemm, D., 1965. Synthesen und Analysen in den Dreiecksdiagrammen FeAsS–CoAsS–NiAsS und FeS2CoS2–NiS2. Neues Jahrbuch fur Mineralogie. Abhandlungen 103, 205–255.

Llanes, A.I., Capote, C., De La Nuez, D., Pacheco, M., Milia, I., Pardo, M., García, I., Petrus, N., Ribada, R., Stout, R., 2006. Informe final sobre los resultados del proyecto I+D 253 evaluación del potential de Au endógeno en ofiolitas de Lomas de Majana, Salomón y Galindo, región Habana-Matanzas y II etapa. Report, Instituto de Geología y Paleontología de Cuba, p. 26p.

Llanes, A.I., Santa Cruz-Pacheco, M., García, I., Morales, A., Palacio, B., Fonseca, E., 2001. Petrología y mineralización de la asociación ofiolítica de Habana-Matanzas (Cuba Occidental). Memorias Geomin 92–101.

Llanes-Castro, A.I., 2016. Constitución y génesis de las ofiolitas de la región de Habana-Matanzas. Unpublished Ph.D. thesis, Universidad de Pinar del Río, p. 250.

Llanes-Castro, A.I., Cruz-Gámez, E.M., Pérez-Rodríguez, M., López-Cruz, O., Furnes, H., 2019. Petrogenesis of plagiogranite and associated diorites and mafic rocks in the Habana–Matanzas ophiolites, northwestern half of central Cuba. J. Geol. Soc. 176, 992–1006. https://doi.org/10.1144/jgs2018-116.

Llanes, A.I., Díaz de Villalvilla, L., Despaigne, A.I., Ronneliah-Sitali, M., García-Jiménez, D., 2015b. Geoquímica de las rocas volcánicas máficas de edad Cretácica de la región de Habana-Matanzas (Cuba Occidental): implicaciones paleotectónicas. Ciencias de la Tierra y el Espacio 16 (2).

Llanes-Castro, A.I., Proenza, J.A., Zaccarini, F., Garuti, G., Pacheco-Sarlabous, M.S.C., 2015. Al-And Cr-rich chromitites from the eastern havana-matanzas ophiolites (western Cuba). Episodes 38, 334–343. https://doi.org/10.18814/epiugs/2015/v38i4/82429.

Lewis, J.F., Draper, G., Proenza, J.A., Espaillat, J., Jiménez, J., 2006. Ophiolite-related ultramafic rocks (serpentinites) in the Caribbean region: a review of their occurrence, composition, origin, emplacement and Ni-laterite soil formation. Geol. Acta 4, 237–263. https://doi.org/10.1344/105.000000368.

Lian, D., Yang, J., Robinson, P.T., Liu, F., Xiong, F., Zhang, L., Gao, J., Wu, W., 2016. Tectonic evolution of the western yarlung zangbo ophiolitic belt, tibet: implications from the petrology, mineralogy, and geochemistry of the peridotites. The Jounral of Geology 124, 353–376. https://doi.org/10.1086/685510.

Liao, S., Tao C, Li, Barriga, F., Liang Yang, W., Yu, J., Zhu, C., 2018. Bulk geochemistry, sulfur isotope characteristics of the Yuhuang-1 hydrothermal field on the ultraslow-spreading Southwest Indian Ridge. Ore Geol. Rev. 96, 13–27. https://doi.org/10.1016/j.oregeorev.2018.04.007.

Linares, E., Osadechy, P., Dovónia, A., 1985. Breve nota explicativa al Mapa Geológico de la República de Cuba a escala 1:500 000. Centro Investigaciones Geológicas. MINBAS, La Habana.

Maffione, M., Van Hinsbergen, D.J.J., Koornneef, L.M.T., Guilmette, C., Hodges, K., Borneman, N., Huang, W., Ding, L., Kapp, P., 2015. Forearc hyperextension dismembered the south Tibetan ophiolites. Geology 43, 475–478. https://doi.org/10.1130/G36472.1.

Marchesi, C., Garrido, C.J., Godard, M., Proenza, J.A., Gervilla, F., Blanco-Moreno, J., 2006. Petrogenesis of highly depleted peridotites and gabbroic rocks from the Mayarı'-Baracoa Ophiolitic Belt (eastern Cuba). Contrib. Mineral. Petrol. 151, 717–736. https://doi.org/10.1007/s00410-006-0089-0.

Marques, A.F.A., Barriga, F., Chavagnac, V., Fouquet, Y., 2006. Mineralogy, geochemistry, and Nd isotope composition of the Rainbow hydrothermal field, Mid-Atlantic Ridge. Miner. Deposita 41, 52–67. https://doi.org/10.1007/s00126-005-0040-8.

Marques, A.F., Barriga, F., Scott, S.D., 2007. Sulfide mineralization in an ultramafic-rock hosted seafloor hydrothermal system: from serpentinization to the formation of Cu-Zn-(Co)-rich massive sulfides. Mar. Geol. 245, 20–39. https://doi.org/10.1016/j.margeo.2007.05.007.

Melchert, B., Devey, C.W., German, C.R., Lackschewitz, K.S., Seifert, R., Walter, M., Mertens, C.R., Yoerger, D.R., Baker, E.T., Paulick, H., Nakamura, K., 2008. First evidence for high-temperature off-axis venting of deep crustal/mantle heat: the Nibelungen hydrothermal field, southern Mid-Atlantic Ridge. Earth Planet Sci. Lett. 275, 61–69. https://doi.org/10.1016/j.epsl.2008.08.010.

Melekestseva, I.Y., Tret'yakov, G.A., Nimis, P., Yuminov, A.M., Maslennikov, V.V., Maslennikova, S.P., Kotlyarov, V.A., Beltenev, V.E., Danyushevsky, L.V., Large, R., 2014. Barite-rich massive sulfides from the Semenov-1 hydrothermal field (Mid-Atlantic Ridge, 13°30.87' N): evidence for phase separation and magmatic input. Mar. Geol. 349, 37–54. https://doi.org/10.1016/j.margeo.2013.12.013.

Melekestseva, I.Y., Zaykov, V.V., Nimis, P., Tret'Yakov, G.A., Tessalina, S.G., 2013. Cu–(Ni–Co–Au)-bearing massive sulfide deposits associated with mafic–ultramafic rocks of the Main Urals Fault, South Urals: geological structures, ore textural and mineralogical features, comparison with modern analogs. Ore Geol. Rev. 52, 18–36. https://doi.org/10.1016/j.oregeorev.2012.03.005.

Mellini, M., Rumori, C., Viti, C., 2005. Hydrothermally reset magmatic spinels in retrograde serpentinites: formation of "ferritchromit" rims and chlorite aureoles. Contrib. Mineral. Petrol. 149, 266–275. https://doi.org/10.1007/s00410-005-0654-y.

Monecke, T., Petersen, S., Hannington, M.D., Grant, H., Samson, I.M., 2016. The minor element endowment of modern sea-floor massive sulfides and comparison with deposits hosted in ancient volcanic successions. Rev. Econ. Geol. 18, 245–306. https://doi.org/10.5382/Rev.18.11.

Morales, A.R., 1987. Informe preliminar sobre la mineralización de oro y platino en la región Habana-Matanzas. Memorias del III Encuentro Científico Técnico de la Filial de Pinar del Río de la Sociedad Cubana de Geología. Instituto Geológico y Paleontológico. Report L-2871.

Morris, A., Anderson, M.W., Omer, A., Maffione, M., Van Hinsbergen, D.J.J., 2017. Rapid fore-arc extension and detachment-mode spreading following subduction initiation. Earth Planet Sci. Lett. 478, 76–88. https://doi.org/10.1016/j.epsl.2017.08.040.

Mozgova, N.N., Trubkin, N.V., Borodaev, Y.S., Cherkashev, G.A., Stepanova, T.V., Semkova, T.A., Uspenskaya, T.Y., 2008. Mineralogy of massive sulfides from the Ashadze hydrothermal field, 13°N, mid-Atlantic Ridge. Can. Mineral. 46, 545–567. https://doi.org/10.3749/canmin.46.3.545.

Nelson, C.E., Proenza, J.A., Lewis, J.F., López-Kramer, J., 2011. The metallogenic evolution of the Greater Antilles. Geol. Acta 9, 229–264. https://doi.org/10.1344/105.000001741.

Nimis, P., Omenetto, P., Buschmann, B., Jonas, P., Simonov, V.A., 2010. Geochemistry of igneous rocks associated with ultramafic–mafic-hosted Cu (Co, Ni, Au) VMS deposits from the Main Uralian Fault (Southern Urals, Russia). Mineral. Petrol. 100, 201–214. https://doi.org/10.1007/s00710-010-0134-6.

Nimis, P., Zaykov, V.V., Omenetto, P., Melekestseva, I.Y., Tesalina, S.G., Orgeval, J.J., 2008. Peculiarities of some mafic-ultramafic- and ultramafic-hosted massive sulfide deposits from the Main Uralian Fault Zone, southern Urals. Ore Geol. Rev. 33, 49–69. https://doi.org/10.1016/j.oregeorev.2006.05.010.

Nimis, P., Tesalina, S.G., Omenetto, P., Tartarotti, P., Lerouge, C., 2004. Phyllosilicate minerals in the hydrothermal mafic–ultramafic-hosted massive-sulfide deposit of Ivanovka (southern Urals): comparison with modern ocean seafloor analogues. Contrib. Mineral. Petrol. 147, 363–383. https://doi.org/10.1007/s00410-004-0565-3.

Ortega, P., 1917. Reseña sobre La Minería en el distrito Central durante el segundo semestre de 1916. Enero 1917 Boletín de minas 3. Fondo geológico Nacional MINBAS, La Habana, Cuba.

Pagé, P., Barnes, S.J., 2009. Using trace elements in Cr-spinels to constrain the origin of podiform chromitites in the thetford mines ophiolite, québec, Canada. Econ. Geol. 104, 997–1018. https://doi.org/10.2113/econgeo.104.7.997.

Palmer, R.H., 1945. Outline of the geology of Cuba. J. Geol. 53 (1), 1–34.

Patten, C.G.C., Coltat, R., Junge, M., Peillod, A., Ulrich, M., Manatschal, G., Kolb, J., 2022. Ultramafic-hosted volcanogenic massive sulfide deposits: an overlooked sub-class of VMS deposits forming in complex tectonic environment. Earth Sci. Rev. 224, 103891 https://doi.org/10.1016/j.earscirev.2021.103891.

Patten, C.G.C., Pitcairn, I.K., Teagle, D.A.H., 2017. Hydrothermal mobilisation of Au and other metals in supra-subduction oceanic crust: insights from the Troodos ophiolite. Ore Geol. Rev. 86, 487–508. https://doi.org/10.1016/j.oregeorev.2017.02.019.

Pearce, J.A., 2008. Geochemical fingerprinting of oceanic basalts with applications to ophiolite classification and the search for Archean oceanic crust. Lithos 100, 14–48. https://doi.org/10.1016/j.lithos.2007.06.016.

Pearce, J.A., 2014. Immobile element fingerprinting of ophiolites. Elements 10 (2), 101–108. https://doi.org/10.2113/gselements.10.2.101.

Petersen, S., Kuhn, K., Kuhn, T., Augustin, N., Hékinian, R., Franz, L., Borowski, C., 2009. The geological setting of the ultramafic-hosted Logatchev hydrothermal field (14°45'N, Mid-Atlantic Ridge) and its influence on massive sulfide formation. Lithos 112, 40–56. https://doi.org/10.1016/j.lithos.2009.02.008.

Proenza, J.A., García-Casco, A., Marchesi, C., Rojas-Agramonte, Y., Lázaro, C., Blanco-Quintero, I., Butjosa, L., Llanes-Castro, I., 2016. Petrology, geochemistry and tectonic setting of ophiolites in Cuba. GSA Annual Meeting in Denver, Colorado, USA –.

Proenza, J., Gervilla, F., Melgarejo, J.C., Bodinier, J.L., 1999. Al-and Cr-rich chromitites from the Mayari-Baracoa ophiolitic belt (eastern Cuba); consequence of interaction between volatile-rich melts and peridotites in suprasubduction mantle. Econ. Geol. 94, 547–566. https://doi.org/10.2113/gsecongeo.94.4.547.

Proenza, J.A., Ortega-Gutiérrez, F., Camprubí, A., Tritlla, J., Elías-Herrera, M., Reyes-Salas, M., 2004. Paleozoic serpentinite-enclosed chromitites from Tehuitzingo (Acatlán Complex, southern Mexico): a petrological and mineralogical study. J. South Am. Earth Sci. 16, 649–666. https://doi.org/10.1016/j.jsames.2003.12.003.

Rui, H., Yang, J., Llanes-Castro, A.I., Zheng, J., Liu, F., Valdes-Mariño, Y., Wu, W., Qiu, T., 2021. Highly refractory harzburgites from the Moa-Baracoa Ophiolitic Massif, Eastern Cuba: insights into forearc mantle melt-rock interactions. Lithos 404–405, 106427. https://doi.org/10.1016/j.lithos.2021.106427.

Russell, N., Moreira, J., Sánchez, R., 2000. Volcanogenic massive sulfide deposits of Cuba. In: Sherlock, R.L., Logan, M.A., Browne, R. (Eds.), Volcanogenic Massive Sulfide Deposits of Latin America. Geological Association of Canada, Mineral Deposits Division, 2 (Special Publications), pp. 241–258.

Semionov, Y.L., Tijomirov, I.N., Lisitsin, A.I., Segura, R., Furrazola, G., 1968. Magmatismo intrusivo y metalogenia de Cuba. Oficina Nacional de Recursos Minerales archive. Report 2451.

Schwarzenbach, E.M., Gazel, E., Caddick, M.J., 2014. Hydrothermal processes in partially serpentinized peridotites from Costa Rica: evidence from native copper and complex sulfide assemblages. Contrib. Mineral. Petrol. 1079 https://doi.org/10.1007/s00410-014-1079-2.

Shanks, W.C.P., Thurston, R., 2012. Volcanogenic Massive Sulfide Occurrence Model: U. S. Geological Survey Scientific Investigations Report 2010–5070–C, p. 345.

Shervais, J.W., 1982. Ti-V plots and the petrogenesis of modern and ophiolitic lavas. Earth Planet Sci. Lett. 59, 101–118. https://doi.org/10.1016/0012-821X(82)90120-0.

Shervais, J.W., 2022. The petrogenesis of modern and ophiolitic lavas reconsidered: Ti-V and Nb-Th. Geosci. Front. 13, 101319 https://doi.org/10.1016/j.gsf.2021.101319.

Tao, C., Li, H., Jin, X., Zhou, J., Wu, T., He, Y., Deng, X., Gu, C., Zhang, G., Liu, W., 2014. Seafloor hydrothermal activity and polymetallic sulfide exploration on the southwest Indian ridge. Chin. Sci. Bull. 59, 2266–2276. https://doi.org/10.1007/s11434-014-0182-0.

Thalhammer, O., Stumpfl, E.F., Panayiotou, A., 1986. Postmagmatic, hydrothermal origin of the sulfide and arsenide mineralizations at Limassol Forest, Cyprus. Miner. Deposita 21, 95–105. https://doi.org/10.1007/BF00204268.

Torres-Zafra, J.L., Cazanas, X., 2021. Mineral systems of Cuba: a panoramic 8 vision of Cuban metallogeny. In: Pardo Echarte, M.E. (Ed.), Geology of Cuba, Regional Geology Reviews. Springer Nature Switzerland AG. https://doi.org/10.1007/978-3-030-67798-5_8255.

Torró, L., Benites, D., Vallance, J., Laurent, O., Ortiz-Benavente, B.A., Chelle-Michou, C., Proenza, J.A., Fontboté, L., 2022. Trace element geochemistry of sphalerite and chalcopyrite in arc-hosted VMS deposits. J. Geochem. Explor. 232, 106882 https://doi.org/10.1016/j.gexplo.2021.106882.

Torró, L., Proenza, J.A., Camprubí, A., Nelson, C.E., Domínguez, H., Carrasco, C., Reynoso-Villafaña, R., Melgarejo, J.C., 2017. Towards a unified genetic model for the Au-Ag-Cu Pueblo Viejo district, central Dominican Republic. Ore Geol. Rev. 89, 463–494. https://doi.org/10.1016/j.oregeorev.2017.07.002.

Torró, L., Proenza, J.A., Espaillat, J., Belén-Manzueta, A.J., Román-Alday, M.C., Amarante, A., González, N., Espinoza, J., Román-Alpiste, M.J., Nelson, C.E., 2018. The discovery of the Romero VMS deposit and its bearing on the metallogenic evolution of Hispaniola during the Cretaceous. Minerals 8, 507. https://doi.org/10.3390/min8110507.

Torró, L., Proenza, J.A., Melgarejo, J.C., Alfonso, P., Farré-de-Pablo, J., Colomer, J.M., García-Casco, A., Gubern, A., Gallardo, E., Cazañas, X., Chávez, C., Del Carpio, R., León, P., Nelson, C.E., Lewis, J.F., 2016. Mineralogy, geochemistry, and sulfur isotope characterization of Cerro de Maimón (Dominican Republic), San Fernando and Antonio (Cuba) lower Cretaceous VMS deposits: formation during subduction initiation of the proto-Caribbean lithosphere within a fore-arc. Ore Geol. Rev. 72, 794–817. https://doi.org/10.1016/j.oregeorev.2015.09.017.

Tourneur, E., Chauvet, A., Kouzmanov, K., Tuduri, J., Paquez, C., Sizaret, S., Karfal, A., Moundi, Y., El Hassani, A., 2021. Co-Ni-arsenide mineralisation in the Bou Azzer district (Anti-Atlas, Morocco): genetic model and tectonic implications. Ore Geol. Rev. 134, 104128 https://doi.org/10.1016/j.oregeorev.2021.104128.

Tremblay, A., Meshi, A., Bédard, J.H., 2009. Oceanic core complexes and ancient oceanic lithosphere: insights from Iapetan and Tethyan ophiolites (Canada and Albania). Tectonophysics 473, 36–52. https://doi.org/10.1016/j.tecto.2008.08.003.

Zaikov, V.V., Melekestseva, I.Y., 2006. The Ishkinino Co-Cu massive sulfide deposit hosted in ultramafic rocks of the main ural fault zone, the southern Urals. Geol. Ore Deposits 48 (3), 151–174. https://doi.org/10.1134/S1075701506030019.

Zasietalev, V., Stepanov, V., 1966. Informe sobre los trabajos geofísicos realizados en junio-noviembre 1966 en la zona Salomón, Guanabacoa, provincia de La Habana. Report 1957. Oficina Nacional de Recursos Minerales archive.